

Journal of the Advanced Program in Plasma Science and Engineering

APPLAuSE

review letters

2020

*P. Cosme
T. C. Dias
P. Estrela
D. Hachmeister
B. Malaca
L. Marques
J. Oliveira
M. Pardal
C. Willim*

*Cover: Spatial profile of the radiation emitted by a spiral beam of particles decelerated due to the conservation of canonical momentum.
by, Miguel Pardal.*

APPLAuSE Review Letters

Editor:

Marta Fajardo

Guest Editor:

Pedro Cosme

May 2020

Contents

Editor Foreword	v
Guest Editor Foreword	v
Best Figure Award	vi
About the Authors	vii
Review Letters	1
Two-dimensional materials plasmonics	1
1 Hydrodynamic Model of Graphene Plasmonics: Dyakonov–Shur Instability and Weak Magnetic Fields <i>Pedro Cosme</i>	
Laser plasma interaction	7
7 Design and implementation of an imaging XUV spectrometer <i>Patrícia Estrela</i>	
11 New acceleration regimes powered by lasers with arbitrary trajectories <i>Bernardo Malaca</i>	
15 Plasma Mirrors: a review <i>Miguel Pardal</i>	
21 Target normal sheath acceleration model <i>Camilla Willim</i>	
Low temperature plasmas	25
25 Kinetic Monte Carlo simulations of plasma chemistry <i>T. C. Dias</i>	
Plasma fusion technology	29
29 ASDEX-Upgrade diagnostics for detachment characterization <i>Daniel Hachmeister</i>	
33 Review of real-time control systems on JET <i>João Oliveira</i>	
Nuclear Detection System	37
37 Assessment of mobile radiation detectors systems considering different scenarios <i>Luís Marques</i>	

Editor Foreword

It is a pleasure to edit yet another issue of APPLAuSE Review Letters, which represents the work performed in the “CTRAN” or Soft Skills course. In a difficult and disruptive time of social distancing through a worldwide pandemic, this year, the CTRAN students are particularly worthy of praise. Although confined to remote meetings, all students were very engaged in the discussions and steadfast in their resolve to improve their communication skills and their career prospects. Their progress was very clear in the oral presentations, and I believe it is also reflected in the quality of the manuscripts published here.

I would like to personally thank all the members of this year’s Soft Skills workshop for this outcome, and this year’s guest editor Pedro Cosme, in particular, for putting together the review. Finally, as always, word of thanks to the anonymous referees from the IPFN, who have been invaluable in their constructive advice.

Marta Fajardo
Instituto de Plasmas e Fusão Nuclear (IPFN), Instituto Superior Técnico
Email: marta.fajardo@tecnico.ulisboa.pt

Guest Editor Foreword

Once again, the new students of the Advanced Program in Plasma Science and Engineering (APPLAuSE) doctoral program of Instituto de Plasmas e Fusão Nuclear (IPFN), joined efforts to write and compile the letters that form this journal. Thus, I am pleased to present to you, as guest editor, the sixth issue of APPLAuSE Review Letters, containing the works of the sixth cohort of APPLAuSE.

This issue of APPLAuSE Review Letters encapsulates in itself the inception of the scientific research of the APPLAuSE PhD students, whose individual scientific careers are now at their first steps and that in the offing will undoubtedly widen the scientific knowledge of Humanity. The articles herein presented are the culmination of the first eight months of learning and labouring of this cohort and already show the scientific areas of choice of each author.

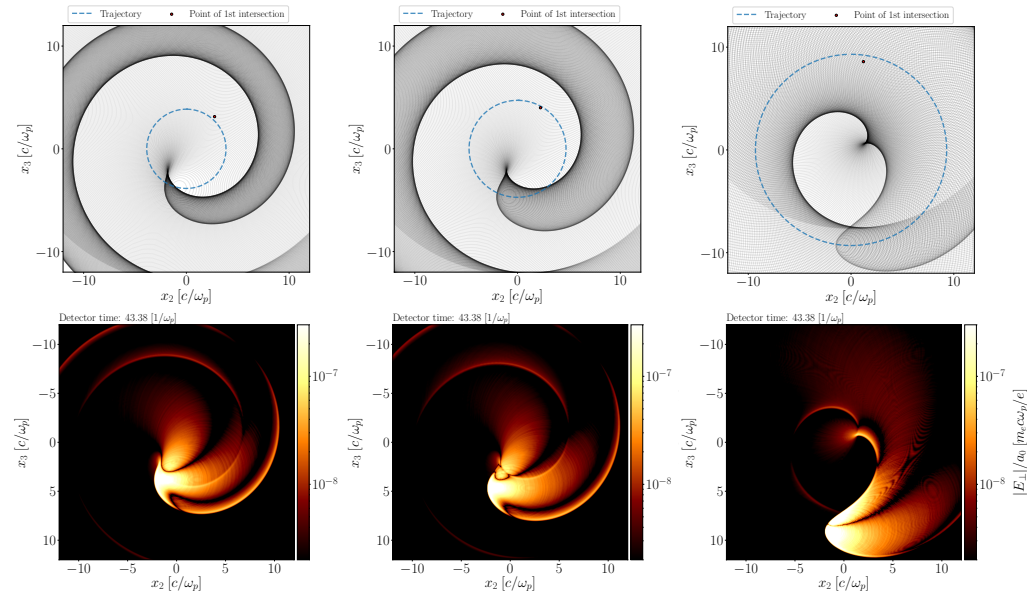
Various distinct articles can be found in this journal. The multiplicity of subjects addressed by the authors bespeaks the diversity and vibrancy found today in plasma physics, a field now spanning a long range, from lasers to two-dimensional materials and nuclear fusion. At APPLAuSE, and within IPFN, the PhD researchers are fortunate to be enrolled in a program that can comprehend all those topics, or others they could envision, concurrently. The editorial team hopes that the reading of this journal shows you precisely this diversity and that you may find in it, not only the research that you are familiar with, but also inspire your inquisitive minds to explore new topics and phenomena in plasma physics.

Ending this foreword, I can not fail to thank the Program Director — Professor João Pedro Bizarro — for all the work that he has done leading this program to the achievements it attained. Also, wishing the next program director — Professor Vasco Guerra — an equally successful term, may he have a gratifying experience.

Pedro Cosme

Best Figure Award

This year the authors elected as best figure the following work from Miguel Pardal.



Spatial profile of the radiation emitted by a spiral beam of particles decelerated due to the conservation of canonical momentum for 3 different spiral radii, r_{spir} . Comparison between simulations (bottom plots) and theoretical models (upper plots).

About the Authors

Pedro Cosme — Guest Editor

 <https://orcid.org/0000-0001-6754-7762>

Pedro Cosme is a PhD student at Instituto de Plasmas e Fusão Nuclear (Lisbon) in the Laboratory for Quantum Plasmas group. Pedro completed his Engineering Physics Masters in 2019, with a dissertation titled “Terahertz plasmonic instabilities in graphene: a hydrodynamical description”. In the present day, he is pursuing his PhD on plasma physics under the supervision of Prof. Hugo Terças. During his academic path, he developed his interest in the fields of plasma physics, particularly on the cross-over to condensed matter physics, nonlinear phenomena and dynamical systems. Currently, his research focuses on plasmonics of graphene and other 2D materials, notably studying its wave instabilities as an active media for the generation of radiation in the THz range.



Tiago C. Dias

 <https://orcid.org/0000-0002-2179-1345>

Tiago Dias is a PhD student at Instituto de Plasmas e Fusão Nuclear in the N-PRiME group. Tiago completed his Engineering Physics Masters in 2019, with a dissertation titled “Atomic oxygen kinetics in CO₂ plasmas”. During his master, he focused on the study of plasma physics, with special emphasis on low-temperature plasmas. Presently, he is working on his PhD on plasma physics under the supervision of Prof. Vasco Guerra. His research is mainly based on plasma modelling, in particular, on the creation of an unified formulation of a gas discharge using Monte Carlo techniques.



Patrícia Estrela

Patrícia Estrela started her PhD journey in 2019, when she joined the APPLAuSE program to pursue research on X-Ray optics and their applications in plasma physics. She is currently a part of the Group of Lasers and Plasmas (GoLP) where she works at the VOXEL laboratory under the supervision of professor Marta Fajardo. Prior to this, she completed her Engineering Physics Masters in 2018 at IST, where she started her work with X-Ray optics.

Daniel Hachmeister

 <https://orcid.org/0000-0002-1420-4376>

Daniel Hachmeister started working in plasma tomography in 2017 for which he obtained his MSc in Engineering Physics at Instituto Superior Técnico (IST), Lisbon, in November 2019. He is currently a PhD student at Instituto de Plasmas e Fusão Nuclear working in plasma reflectometry and, more broadly, in divertor physics. His work is split between IST in Portugal and ASDEX-Upgrade in Germany, where he joins the Medium Size Tokamak campaign.



Bernardo Malaca

Bernardo Malaca is a PhD student at Instituto de Plasmas e Fusão Nuclear in the Extreme Plasma Physics group. Bernardo completed his Engineering Physics Masters in 2018, on “Machine Learning Controlled Plasma Based Acceleration”. During his master he applied machine learning concepts to optimize laser wakefield acceleration at the simulation level. Currently, his research is based on laser wavefront shaping to enhance several laser-plasma interactions, from acceleration to radiation emission.



Luís Marques

 <https://orcid.org/0000-0003-1965-2044>

Luís Marques is a PhD student at Centro de Investigação da Academia da Força Aérea. Luís completed his Engineering Physics Masters in 2011, on “Comparative study of HPGe, NaI(Tl), CdZnTe detectors for Security applications and for Nuclear and Radiological threats”. Currently, he is a researcher at CIAFA, a collaborative researcher at Centro de Ciências e Tecnologias Nucleares (C2TN), Unmanned Aircraft System (UAS) operator, professor of Aerodynamics at Portuguese Air Force Academy and participates in R&D project FRIENDS. His interest research area is on radiation detection systems to be used in UAS.



João Oliveira

 <https://orcid.org/0000-0002-2784-214X>

João Oliveira is a PhD student Instituto de Plasmas e Fusão Nuclear (Lisbon) in the Engineering and Systems Integration group. He completed his Master’s degree in 2019 with a dissertation titled “Spherical Rotor asynchronous motor control by 3D variable frequency drive”. Currently he is working on his PhD under the supervision of Prof. Horácio Fernandes where he is developing control hardware for the next generation of tokamak fusion machines.

Miguel Pardal

 <https://orcid.org/0000-0001-9588-1100>

Born 1995 near Lisbon, started an internship in the the Group of Lasers and Plasmas in 2017 under the supervision of Prof. Jorge Vieira to contribute to the production of educational tools for plasma physics. Developed his master’s thesis in the same group, working on a simulation tool to obtain the radiation emitted in plasma particle-in-cell simulations called Radiation Diagnostic for OSIRIS. Currently doing a PhD in the Group of Lasers and Plasmas exploiting the possibilities offered by the aforementioned tool to explore radiation generation scenarios in plasmas under the supervision of Jorge Vieira.



Camilla Willim

Camilla received her master’s degree in physics in 2018 at the Heinrich-Heine University in Düsseldorf (HHU), Germany. Her master’s project was directly related to laser–plasma physics and under the supervision of PD Dr. Götz Lehmann. She investigated two-dimensional plasma photonic crystals — plasma structures with unique optical properties. Camilla is currently a graduate student at IST. She is pursuing her PhD in the Group for Lasers and Plasmas (GoLP) under the supervision of Prof. Jorge Vieira and Prof. Luís O. Silva. Camilla’s work focusses on non-linear optics of plasmas in the critical density limit at high intensities driven by structured light.



Hydrodynamic Model of Graphene Plasmonics: Dyakonov–Shur Instability and Weak Magnetic Fields*

Pedro Cosme¹

Abstract—Several hydrodynamic descriptions of charge transport in graphene have been presented in the late years. This work briefly presents a general hydrodynamic model of the electronic 2D fluid in the Fermi liquid and slow drift regime, with particular emphasis in plasmons in graphene transistors. Attention is drawn to the correction of the convective term in Euler equation, which arises from the varying effective mass. Furthermore, the Dyakonov–Shur instability in graphene is analysed and extended to include the effects of weak magnetic fields. In that circumstances our numerical results evince that the growth rate of the instability decreases with the magnetic field strength.

I. INTRODUCTION

In recent years, the scientific community has witnessed the emergence of bidimensional materials technology. In this field graphene is undoubtedly one of the most prominent materials. Among the many applications of graphene, the possibility of resorting to plasmonics instabilities to trigger the emission, or conversely, the detection, of THz radiation has been an active field of study [1–4].

One of the defining characteristics of graphene is its high electron mobility, which emanates from the scarcity of electron scattering with phonons, defects, or impurities; which leads to large electron–impurity mean free path ℓ_{imp} . Indeed, ultra-clean samples of graphene encapsulated by hexagonal boron nitride (hBN) [5] or hBN–graphene–WSe₂ structures [6] exhibit a mobility $\mu > 3.5 \times 10^5 \text{ cm}^2 \text{ V}^{-1} \text{ s}^{-1}$. Yet, the electron–electron scattering is significant, resulting in a short mean free path ℓ_{ee} at room temperature. Thereby, it is possible to design a system with dimension L under the restraint $\ell_{ee} \ll L \ll \ell_{\text{imp}}$. In such a regime, the collective behaviour of carriers can be adequately modelled by a hydrodynamic description [2, 7–11], with some recent experimental results validating this approach [12–14].

Given the relativistic Hamiltonian of single-layer graphene (SLG) carriers, a relativistic description is required for velocities near the Fermi velocity v_F . However, the explored mechanisms for the creation and control of plasmons in graphene customarily rely on graphene channel field-effect transistors (GFET), which allow to readily control the Fermi level, and where the velocity of the carriers is expected to saturate [15–17] far bellow such values. Thus, the model hereinafter presented focuses on the small velocities regime $v \ll v_F$, to describe the plasmonic excitations within graphene in the Fermi-liquid regime where $E_F \gg k_B T$.

*This work was supported by Fundação para a Ciência e Tecnologia

¹P. Cosme is with Instituto de Plasmas e Fusão Nuclear, Instituto Superior Técnico, 1049-001 Lisboa, Portugal pacsilva@ipfn.tecnico.ulisboa.pt

Indeed, for electronic applications, it is reasonable to expect the Fermi level to be large enough to prevent interband transitions.

This work briefly reviews the general assumptions for hydrodynamic modelling of electronic transport in graphene in the aforementioned conditions, with particular emphasis in GFETs. Furthermore, the Dyakonov–Shur instability in graphene is analysed and extended to include the effects of weak magnetic fields.

II. GENERAL FLUID MODEL

A. Definition of an effective mass.

The fact that the electrons in graphene behave as massless Dirac fermions poses the major difficulty for the development of hydrodynamic models. In SLG, not only carriers have zero mass, but also the effective inertial mass tensor diverges [18]. A naive approach would dictate to define mass as,

$$m^* = \frac{\hbar k_F}{v_F} = \frac{\hbar \sqrt{\pi n}}{v_F}, \quad (1)$$

where $\hbar k_F$ is the Fermi momentum and n is the carrier number density. This definition is used extensively in the literature [7, 9, 10] to address the issue. It is important to note that, since the electronic fluid is compressible, the effective mass is not a conserved quantity, contrary to customary fluids.

B. Fluid model from kinetic theory

Starting from the Boltzmann equation for the distribution function f

$$\frac{\partial}{\partial t} f + \mathbf{v} \cdot \nabla_r f + \mathbf{F} \cdot \nabla_p f = \hat{\mathcal{C}}[f], \quad (2)$$

one can derive the hydrodynamic model for electronic transport in SLG. Here, the collision operator can be taken, in the Bhatnagar–Gross–Krook approximation [19, 20], as $\hat{\mathcal{C}}[f] = (f_{\text{Equilibrium}} - f)/\tau$, and since we are interested in mesoscopic effects, with small Knudsen number, and time scales much longer than the collision time, $\hat{\mathcal{C}}[f] \approx 0$. This statement does not mean that there are no collisions in the electronic fluid, but that the time scale of the electron–electron interactions is fast enough to maintain the distribution function in equilibrium.

Integrating the zero-order momentum of (2), yields the continuity equation

$$\frac{\partial n}{\partial t} + \frac{\partial}{\partial x_i} n v_i = 0, \quad (3)$$

as usual, corresponding to the conservation of particles, and thus charge. Furthermore, the first momentum of (2) simplifies to

$$\frac{\partial v_i}{\partial t} + \frac{1}{2}v_j \frac{\partial v_i}{\partial x_j} + \frac{1}{nm^*} \frac{\partial P_{ij}}{\partial x_j} - \frac{1}{m^*} F_i = 0, \quad (4)$$

where P_{ij} is the pressure stress tensor and F_i the external forces. Thus, the variation of the effective mass introduces a correction to the convective term. (cf. Appendix A)

C. Electron degeneracy pressure

Besides the description of the effective mass, the dependency of pressure with the density is key to the development of a consistent model of electrons, as they are subject to high degeneracy pressure.

Regarding the *hydrostatic* diagonal terms of P_{ij} , the pressure in the 2D Fermi-Dirac system [7, 21, 22] is given by

$$P = \frac{2(k_B T)^3}{\pi \hbar^2 v_F^2} \mathfrak{F}_2 \left(\frac{E_F}{k_B T} \right), \quad (5)$$

where \mathfrak{F}_2 is the complete Fermi-Dirac integral and the dependency of the chemical potential with the temperature was discarded, as $T \ll T_F$. Furthermore, such relation can be expanded for the Fermi liquid regime $E_F \gg k_B T$

$$P(E_F) = \frac{E_F^3}{3\pi(\hbar v_F)^2} + \mathcal{O} \left(\frac{k_B T}{E_F} \right)^2 = \frac{\hbar v_F}{3\pi} (\pi n)^{\frac{3}{2}} \quad (6)$$

hence, the pressure term in (4) reduces to

$$\frac{1}{nm^*} \frac{\partial P}{\partial x_j} = \frac{v_F^2}{2n} \frac{\partial n}{\partial x_j} \quad (7)$$

D. Inviscid limit

In (4), the off-diagonal elements of the pressure tensor P_{ij} describe the viscous terms of the fluid. In SLG the dynamic viscosity $\nu = v_F \ell_{ee}/4$ [10, 11, 23, 24]. Therefore the Reynolds number of the electronic fluid is

$$\text{Re} = \frac{4Lv_0}{\ell_{ee}v_F}. \quad (8)$$

Whereas $v_0/v_F \ll 1$ for our assumptions about the relativistic limit to hold, the ratio L/ℓ_{ee} is required to be large enough for the hydrodynamic approach be valid. So, by a clever choice of parameters, the Reynolds number can be tailored to be high enough for the viscous effects to be negligible. Hence, the present discussion will be limited to the inviscid regime, in which the fluid equations take the form

$$\frac{\partial n}{\partial t} + \nabla \cdot n\mathbf{v} = 0 \quad (9a)$$

$$\frac{\partial \mathbf{v}}{\partial t} + \frac{1}{2}(\mathbf{v} \cdot \nabla)\mathbf{v} + \frac{v_F^2}{2n} \nabla n - \frac{\mathbf{F}}{m^*} = 0. \quad (9b)$$

III. PLASMONS IN UNGATED GRAPHENE

Despite the simplicity of the previous model, it correctly describes the behaviour of collective charge plasmons in graphene. Expanding the density as $n = n_0 + n_1(x, t)$ and taking the two dimensional Fourier transform of (9) keeping only linear terms yields

$$\omega \tilde{n}_1 - \mathbf{k} n_0 \tilde{\mathbf{v}}_1 = 0 \quad (10a)$$

$$\omega \tilde{\mathbf{v}}_1 - \mathbf{k} \frac{v_F^2}{2n_0} \tilde{n}_1 + \mathbf{k} \frac{ev_F}{\hbar\sqrt{\pi n_0}} \tilde{\phi} = 0 \quad (10b)$$

where the tilde indicates Fourier transform and ϕ is the Coulomb potential, given by

$$\tilde{\phi}(\mathbf{k}) = -\frac{e}{2\epsilon} \frac{\tilde{n}(\mathbf{k})}{|\mathbf{k}|}. \quad (11)$$

Considering, for simplicity, k -vectors only along one direction and combining (10) with (11) the well-known dispersion relation for SLG plasmons is retrieved:

$$\frac{\hbar\omega}{E_F} = \sqrt{\frac{1}{2} \frac{k^2}{k_F^2} + 2\alpha} \frac{k}{k_F} \quad (12)$$

where $\alpha = e^2/4\pi\epsilon\hbar v_F$ is the fine structure constant of graphene.

IV. ACOUSTIC PLASMONS IN GATED GRAPHENE

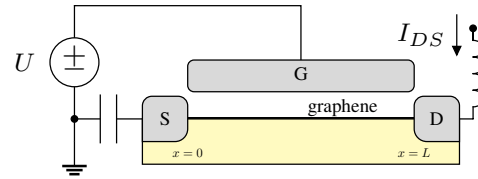


Fig. 1. Schematic representation of a graphene channel field-effect transistor with a top gate (G). The presented setup also shows the Dyakonov-Shur impedance realisation at source (S) and drain (D).

In most of the technological applications in the area of electronics and photonics, graphene layers are subject to an external electric potential, usually imposed by one or more metallic gates. The behaviour of the electronic fluid in this configuration is, therefore, of substantial relevance.

Considering a SLG in a field effect transistor (FET) structure, i.e. placed between two metallic contacts, source, and drain, and subject to a gate (cf. Fig. 1), the electric force in the electrons is dominated by the imposed potential that screens the Coulomb interaction between them. Therefore, the acceleration of electrons is solely due to the imposed potential. Moreover, in the gradual channel approximation, the Fermi level varies slowly along the dimensions of the transistor, and so the field can be considered uniform and akin to a plane capacitor. The applied bias potential U_{gate} has the contribution of both the geometric capacitance from the gate C_g and the quantum capacitance C_q [25, 26] as

$$U_{\text{gate}} = en \left(\frac{1}{C_g} + \frac{1}{C_q} \right) \approx \frac{en}{C_g}. \quad (13)$$

since for typical carrier densities $n \gtrsim 10^{12} \text{ cm}^{-2}$ quantum capacity dominates $C_q \gg C_g$. The relation (13) provides a way to control the excess carrier density, and so the Fermi level, without resorting to doping. Moreover, as $\nabla U_{\text{gate}} = \nabla \phi$, it closes the set of equations (9).

A. Linear dispersion plasmons

The geometric capacitance in the parallel plates approximation is given by $C_g = \varepsilon/d_0$, where d_0 is the separation and ε the medium permittivity. Consequently, (9b) now reads

$$\frac{\partial \mathbf{v}}{\partial t} + \frac{1}{2}(\mathbf{v} \cdot \nabla)\mathbf{v} + \frac{v_F^2}{2n} \nabla n + \frac{S^2}{\sqrt{n_0 n}} \nabla n = 0 \quad (14)$$

where $S^2 = \frac{e^2 d v_F \sqrt{n_0}}{\varepsilon \hbar \sqrt{\pi}}$, which can be interpreted as the sound velocity for the plasmons.

Assuming that the dynamics of the system is predominantly one-dimensional, linearising the the fluid model with a drift constant velocity v_0 as $v = v_0 + v_1(x, t)$, yields the following dispersion relation:

$$(\omega - kv_0) \left(\omega - \frac{kv_0}{2} \right) = \underline{S}^2 k^2, \quad (15)$$

where $\underline{S}^2 = S^2 + v_F^2/2$, can be retrieved. Therefore, in the gated regime, the plasmons in SLG are akin to acoustic waves propagating with velocity \underline{S} . It is important to note that this velocity \underline{S} is the phase velocity of the perturbations on the electronic fluid and so it is not bounded by the Fermi velocity. In fact, for the plasmons to prevail, their phase velocity must surpass v_F , in order to not be in a Landau damping regime. While this analysis is intended for small drift velocities $v_0 \ll v_F$, for the typical physical parameters of a GFET, the ratio \underline{S}/v_0 scales up to a few tens, and thus one can obtain $S > v_F$.

B. Quantum capacitance effects

The quantum capacitance C_q reflects the change in potential with the occupancy of the band structure of the material [27, 28] and is defined as

$$C_q = -e \frac{\partial Q}{\partial E_F} = e^2 \frac{2k_B T}{\pi v_F^2 \hbar^2} \log 2 \left(1 + \cosh \frac{E_F}{k_B T} \right) \quad (16)$$

which in the Fermi liquid regime reduces to

$$C_q = 2e^2 \sqrt{\pi n} / \pi \hbar v_F. \quad (17)$$

Therefore, wishing to take into account the quantum capacitance effect the acceleration term in (9b) becomes

$$-\frac{e}{m} \nabla \phi = \frac{e^2 d_0 v_F}{\varepsilon \hbar \sqrt{\pi n}} \nabla n + \frac{v_F^2}{4n} \nabla n \quad (18)$$

and so, the contribution from the quantum capacitance can be added as a correction to the pressure term, slightly enhancing the sound speed of the plasmon waves $\underline{S}^2 = S^2 + 3v_F^2/4$.

V. DYAKONOV–SHUR INSTABILITY

The hydrodynamic model in (9) contains an instability under the boundary conditions of fixed density at the source $n(x=0) = n_0$ and fixed current density at the drain $n(x=L)v(x=L) = n_0 v_0$, dubbed in the literature as the Dyakonov–Shur (DS) instability [29, 30]. The latter arises from the multiple reflections of the plasma waves at the boundaries, which provide positive feedback for the incoming waves driven by the current at the drain. From an electronic point of view, the peculiar boundary conditions correspond to an AC short circuit at the source, forcing the voltage (and so the carriers density) to remain constant, and an AC open circuit at the drain setting the current constant [31, 32]. Thus, this can be implemented with a low-reactance capacitor on the source and a high-reactance inductor on the drain [33], as outlined in Figure 1.

The asymmetric boundary conditions described above imply that the counterpropagating wave vectors need to comply with the relation

$$\frac{k_+}{k_-} = e^{i(k_+ - k_-)L}. \quad (19)$$

This leads to the frequency to become complex, $\omega = \omega_r + i\gamma$, where ω_r is the electron oscillation frequency and γ is the instability growth rate [29, 31, 34], which are given by

$$\begin{aligned} \omega_r &= \frac{|\underline{S}^2 - (\frac{3}{4}v_0)^2|}{2L\underline{S}} \pi, \\ \gamma &= \frac{\underline{S}^2 - (\frac{3}{4}v_0)^2}{2L\underline{S}} \log \left| \frac{\underline{S} + \frac{3}{4}v_0}{\underline{S} - \frac{3}{4}v_0} \right|. \end{aligned} \quad (20)$$

Therefore, it is clear that the plasmonic oscillations become unstable, having a positive growth rate, for $S/v_0 > 3/4$, a *subsonic* regime where drift velocity is lower than the S parameter. This eliminates the need for high drift velocities of the carriers, and the frequency and growth rate of the waves are rather dominated by the S/L value. Moreover, given the dependence of S with gate voltage, and as $v_0 n_0 \sim I_{\text{DS}}/W e$, with I_{DS} representing the source-to-drain current and W the transverse width of the sheet, the frequency can be tuned by the gate voltage and injected drain current, not being solely restricted to the geometric factors of the FET.

VI. INCLUSION OF WEAK MAGNETIC FIELDS

In the presence of strong magnetic fields, the Fermi–Dirac systems are extremely modified, and several phenomena, vastly studied in the last years, arise. However, such fields $\gtrsim 1\text{T}$ are not adequate for room-temperature and integrated circuit technology. Instead, this section deals with the influence of weak fields in the vicinity of the graphene layer.

A. Plasmons with $\mathbf{k} \perp \mathbf{B}$

Considering an uniform field $\mathbf{B} = B_0 \hat{z}$ perpendicular to the graphene layer and writing $\mathbf{v} = v_x \hat{x} + v_y \hat{y}$ while looking for propagation along x , $\mathbf{k} = k \hat{x}$, the system (9) becomes,

in Fourier space,

$$(\omega - kv_0) \tilde{n}_1 = kn_0 \tilde{v}_x \quad (21a)$$

$$\left(\omega - \frac{kv_0}{2}\right) \tilde{v}_x = k \frac{S^2}{n_0} \tilde{n}_1 - i\omega_c \tilde{v}_y \quad (21b)$$

$$\omega \tilde{v}_y = i\omega_c \tilde{v}_x \quad (21c)$$

where $\omega_c = eB/m^*$ is the cyclotron frequency. Note that as the mass is much smaller than the electron mass it is possible to access high cyclotron frequencies with modest fields; for a typical excess density of 10^{12} cm^{-2} $\omega_c/B = 9 \text{ THz T}^{-1}$. Furthermore, combining (21) yields the dispersion relation

$$(\omega - kv_0) \left(\omega - \frac{kv_0}{2} - \frac{\omega_c^2}{\omega}\right) = S^2 k^2. \quad (22)$$

With this dispersion relation, the propagating solutions $\omega_{\pm}(k)$ coalesce to ω_c as $k \rightarrow 0$, opening a gap at the origin as patent in Fig. 2, whereas for large k we recover the unperturbed solutions $\omega \simeq (3/4v_0 \pm S)k$. Moreover, a third nonmonotonic solution $\omega_0(k)$ is also present; since $\lim_{S/v_0 \rightarrow \infty} \omega_0(k) = 0$ such solution has little interest for the discussed subsonic regime.

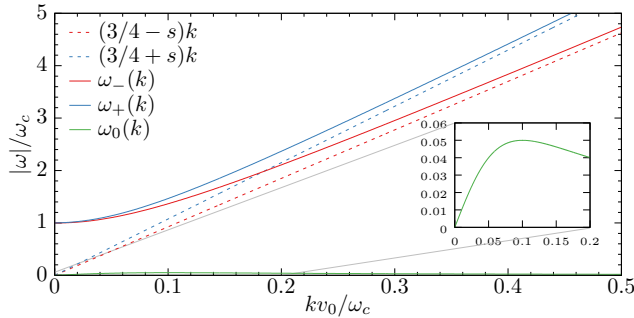


Fig. 2. Solutions of dispersion relation (22) with $S/v_0 = 10$ (solid lines) alongside the solutions in the absence of magnetic field (dashed lines). Inset: Detail of the third solution, showing its maximum at $(v_0/S, v_0/2S)$.

B. Influence in Dyakonov–Shur instability

Returning to (22) and writing ω in v_0/L units, k in $1/L$ and $s = S/v_0$ one gets

$$(\omega - k) \left(\omega - \frac{k}{2} - \frac{\omega_c^2}{\omega}\right) = s^2 k^2 \quad (23)$$

and the solutions for the wave vector are

$$k_{\pm} = \frac{3\omega \mp \omega \sqrt{1 + 16s^2 - (4s^2 + 1) \frac{4\omega_c^2}{\omega^2} + \frac{4\omega_c^4}{\omega^4}} - 2\frac{\omega_c^2}{\omega}}{(2 - 4s^2)} \quad (24)$$

Then, numerically solving the condition of (19) provides the results presented in Fig. 3. Therefore, contrarily to what has been previously reported [35] for regular FETs, it is clear that, even far from resonance, the growth rate of the instability decreases; although without significant influence in the frequency. The reason for our results to differ from those presented in [35] lies in treatment of the wave vector solutions. In the cited work the cyclotron frequency ω_c is continuously normalised to the instability frequency ω itself. Such approach simplifies the problem as it artificially

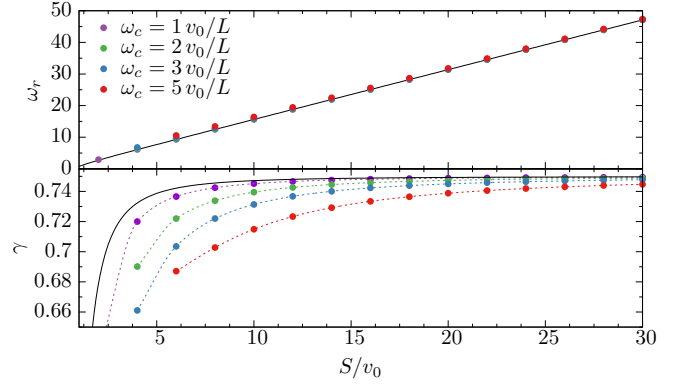


Fig. 3. Numerical solutions for frequency and growth rate (in units of v_0/L) of Dyakonov–Shur instability for several cyclotron frequencies ω_c (coloured dots) and analytical solution (20) corresponding to $B = 0$ (solid line). Although there is no significant change in the real part of the frequency, the growth rate diminishes slightly.

linearises (24). However, this obscures the analysis as in a ω vs. S plot the cyclotron frequency would be also varying. Moreover, from a technological point of view it is not reasonable to expect that the external field could continuously adjust to the plasmon frequency. Oppositely, in our numerical solutions all the quantities are normalised to static system parameters; hence, having ω_c independent of ω .

VII. FINAL REMARKS

The theoretical study of electronic transport in graphene is a challenging task, covering several regimes and interactions, and resorting to complex techniques. Nonetheless, the hydrodynamic models provide a semi-classical description capable of recovering the behaviour and properties of such quantum fluids while also allowing numerical simulation with well-established methods. This work presented the main approach to obtain such a description in the fully degenerate Fermi liquid regime, and in the future, it can be extended to other conditions such as the Dirac fluid.

However, it is vital to stress that conventional fluid equations — for instance Euler equation — cannot be bluntly applied and that the variation of the effective mass with the numerical density introduces a correction in the nonlinear convective term, breaking the symmetry of the dispersion relation in the presence of a base drift of the fluid.

Besides the renewed analysis of the DS instability, the presented hydrodynamic model showed that the presence of a weak transverse magnetic field dramatically changes the nature of the plasmons for small k . Moreover, our numerical results point out that the magnetic field impairs the growing of the DS instability, a result that, to our knowledge, have not yet been reported in this context. Nonetheless, full two-dimensional simulations must be performed in order to study the influence of such fields beyond the linear theory and in particular its effects on the amplitude of the nonlinear waves.

APPENDIX

A. Derivation of momentum equation from Boltzmann equation

The first momentum of the Boltzmann equation (2) returns

$$\frac{\partial}{\partial t}(\rho v_i) + \frac{\partial}{\partial x_j}(\rho v_i v_j) + \frac{\partial}{\partial x_j} P_{ij} - n F_i = 0. \quad (25)$$

However, this conservation of momentum needs to be analysed with care as the mass dependency with the density introduces a quantitative correction to the Euler equation. Since $m^* = \hbar\sqrt{\pi n}/v_F$, (25) leads to

$$\begin{aligned} & \frac{\hbar\sqrt{\pi}}{v_F} n^{3/2} \frac{\partial v_i}{\partial t} + \frac{\hbar\sqrt{\pi}}{v_F} \frac{3}{2} n^{1/2} v_i \frac{\partial n}{\partial t} + \\ & + v_i \frac{\hbar\sqrt{\pi}}{v_F} n^{3/2} \frac{\partial v_j}{\partial x_j} + v_i v_j \frac{\hbar\sqrt{\pi}}{v_F} \frac{3}{2} n^{1/2} \frac{\partial n}{\partial x_j} + \\ & + \frac{\hbar\sqrt{\pi}}{v_F} n^{3/2} v_j \frac{\partial v_i}{\partial x_j} + \frac{\partial P_{ij}}{\partial x_j} - n F_i = 0 \end{aligned} \quad (26)$$

where replacing the $\frac{\partial n}{\partial t}$ term from (3) simplifies to

$$\frac{\partial v_i}{\partial t} + \frac{1}{2} v_j \frac{\partial v_i}{\partial x_j} + \frac{1}{nm^*} \frac{\partial P_{ij}}{\partial x_j} - \frac{1}{m^*} F_i = 0. \quad (27)$$

Therefore, revealing the 1/2 correction that arises from the non-constant effective mass.

ACKNOWLEDGMENT

The author acknowledges the funding provided by FCT-Portugal through the grant number PD/BD/150415/2019.

REFERENCES

- [1] S. Hosseinijad, R. Faraji-Dana, S. Abadal, M. Lemme, P. Haring Bolívar, E. Alarcón, M. Neshat, and A. Cabellos-Aparicio, "Reconfigurable THz Plasmonic Antenna Based on Few-Layer Graphene with High Radiation Efficiency," *Nanomaterials*, vol. 8, no. 8, p. 577, 2018.
- [2] C. B. Mendl, M. Polini, and A. Lucas, "Coherent Terahertz Radiation from a Nonlinear Oscillator of Viscous Electrons," *arXiv preprint*, pp. 1–8, 9 2019.
- [3] A. K. Wigger, S. E. Hosseinijad, S. Abadal, E. Alarcón, D. Stock, M. Lemme, S. Schaeffer, C. Suessmeier, S. Wagner, P. H. Bolívar, and A. Cabellos-Aparicio, "A Graphene Based Plasmonic Antenna Design for Communication in the THz Regime," in *Conference on Lasers and Electro-Optics*, 2017, p. JTh2A.37.
- [4] T. Otsuji, V. Popov, and V. Ryzhii, "Active graphene plasmonics for terahertz device applications," *Journal of Physics D: Applied Physics*, vol. 47, no. 9, 2014.
- [5] J. Son, J. Kwon, S. Kim, Y. Lv, J. Yu, J.-Y. Lee, H. Ryu, K. Watanabe, T. Taniguchi, R. Garrido-Menacho, N. Mason, E. Ertekin, P. Y. Huang, G.-H. Lee, and A. M. van der Zande, "Atomically precise graphene etch stops for three dimensional integrated systems from two dimensional material heterostructures," *Nature Communications*, vol. 9, no. 1, p. 3988, 12 2018.
- [6] L. Banszerus, T. Sohier, A. Epping, F. Winkler, F. Libisch, F. Haupt, K. Watanabe, T. Taniguchi, K. Müller-Caspary, N. Marzari, F. Mauri, B. Beschoten, and C. Stampfer, "Extraordinary high room-temperature carrier mobility in graphene-WSe₂ heterostructures," pp. 1–15, 9 2019.
- [7] A. J. Chaves, N. M. R. Peres, G. Smirnov, and N. A. Mortensen, "Hydrodynamic model approach to the formation of plasmonic wakes in graphene," *Physical Review B*, vol. 96, no. 19, p. 195438, 11 2017.
- [8] B. N. Narozhny, I. V. Gornyi, A. D. Mirlin, and J. Schmalian, "Hydrodynamic approach to electronic transport in graphene," *Annalen der Physik*, vol. 529, no. 11, pp. 1–12, 2017.
- [9] D. Svintsov, V. Vyurkov, V. Ryzhii, and T. Otsuji, "Hydrodynamic electron transport and nonlinear waves in graphene," *Physical Review B*, vol. 88, no. 24, p. 245444, 12 2013.
- [10] A. Lucas and K. C. Fong, "Hydrodynamics of electrons in graphene," *Journal of Physics Condensed Matter*, vol. 30, no. 5, 2018.
- [11] M. Müller, J. Schmalian, and L. Fritz, "Graphene: A Nearly Perfect Fluid," *Physical Review Letters*, vol. 103, no. 2, p. 025301, 7 2009.
- [12] J. A. Sulpizio, L. Ella, A. Rozen, J. Birkbeck, D. J. Perello, D. Dutta, M. Ben-Shalom, T. Taniguchi, K. Watanabe, T. Holder, R. Queiroz, A. Principi, A. Stern, T. Scaffidi, A. K. Geim, and S. Ilani, "Visualizing Poiseuille flow of hydrodynamic electrons," *Nature*, vol. 576, no. 7785, pp. 75–79, 12 2019.
- [13] J. Mayzel, V. Steinberg, and A. Varshney, "Stokes flow analogous to viscous electron current in graphene," *Nature Communications*, vol. 10, no. 1, 2019.
- [14] A. I. Berdyugin, S. G. Xu, F. M. D. Pellegrino, R. Krishna Kumar, A. Principi, I. Torre, M. Ben Shalom, T. Taniguchi, K. Watanabe, I. V. Grigorieva, M. Polini, A. K. Geim, and D. A. Bandurin, "Measuring Hall viscosity of graphene's electron fluid," *Science*, vol. 364, no. 6436, p. eaau0685, 2 2019.
- [15] Q. Wilmart, M. Boukhicha, H. Graef, D. Mele, J. Palomo, M. Rosticher, T. Taniguchi, K. Watanabe, V. Bouchiat, E. Baudin, J. M. Beroir, E. Bocquillon, G. Fève, E. Pallecchi, and B. Plaçais, "High-frequency limits of graphene field-effect transistors with velocity saturation," *Applied Sciences (Switzerland)*, vol. 10, no. 2, 2020.
- [16] M. A. Yamoah, W. Yang, E. Pop, and D. Goldhaber-Gordon, "High-Velocity Saturation in Graphene Encapsulated by Hexagonal Boron Nitride," *ACS Nano*, vol. 11, no. 10, pp. 9914–9919, 10 2017.
- [17] V. E. Dorgan, M.-H. Bae, and E. Pop, "Mobility and saturation velocity in graphene on SiO₂," *Applied Physics Letters*, vol. 97, no. 8, p. 082112, 8 2010.
- [18] N. W. Ashcroft and N. D. Mermin, *Solid state physics*. Holt, Rinehart and Winston, 1976.
- [19] M. Rieutord, *Fluid Dynamics*, ser. Graduate Texts in Physics. Cham: Springer International Publishing, 2015, vol. 44, no. 12.
- [20] F. Haas, *Quantum Plasmas*, ser. Springer Series on Atomic, Optical, and Plasma Physics. New York, NY: Springer New York, 2011, vol. 65, no. 9.
- [21] L. Landau and E. Lifshitz, "Courses on theoretical physics: Statistical Physics, Part 1," 1976.
- [22] G. Giuliani and G. Vignale, *Quantum Theory of the Electron Liquid*. Cambridge University Press, 2005.
- [23] I. Torre, A. Tomadin, A. K. Geim, and M. Polini, "Nonlocal transport and the hydrodynamic shear viscosity in graphene," *Physical Review B - Condensed Matter and Materials Physics*, vol. 92, no. 16, pp. 1–12, 10 2015.
- [24] L. Levitov and G. Falkovich, "Electron viscosity, current vortices and negative nonlocal resistance in graphene," *Nature Physics*, vol. 12, no. 7, pp. 672–676, 7 2016.
- [25] W. Zhu, V. Perebeinos, M. Freitag, and P. Avouris, "Carrier scattering, mobilities, and electrostatic potential in monolayer, bilayer, and trilayer graphene," *Physical Review B*, vol. 80, no. 23, p. 235402, 12 2009.
- [26] S. Das Sarma, S. Adam, E. H. Hwang, and E. Rossi, "Electronic transport in two-dimensional graphene," *Reviews of Modern Physics*, vol. 83, no. 2, pp. 407–470, 5 2011.
- [27] T. Fang, A. Konar, H. Xing, and D. Jena, "Carrier statistics and quantum capacitance of graphene sheets and ribbons," *Applied Physics Letters*, vol. 91, no. 9, p. 092109, 8 2007.
- [28] S. Dröschner, P. Roulleau, F. Molitor, P. Studerus, C. Stampfer, K. Ensslin, and T. Ihn, "Quantum capacitance and density of states of graphene," *Physica Scripta*, vol. T146, no. T146, p. 014009, 1 2012.
- [29] M. Dyakonov and M. Shur, "Shallow water analogy for a ballistic field effect transistor: New mechanism of plasma wave generation by dc current," *Physical Review Letters*, vol. 71, no. 15, pp. 2465–2468, 10 1993.
- [30] M. I. Dyakonov, "Generation and detection of Terahertz radiation by field effect transistors," *Comptes Rendus Physique*, vol. 11, no. 7–8, pp. 413–420, 8 2010.
- [31] F. J. Crowne, "Contact boundary conditions and the Dyakonov–Shur instability in high electron mobility transistors," *Journal of Applied Physics*, vol. 82, no. 3, pp. 1242–1254, 8 1997.
- [32] B. Barut, G. R. Aizin, E. Einarsson, J. M. Jornet, T. Sugaya, and J. P. Bird, "Realizing Asymmetric Boundary Conditions for Plasmonic THz Wave Generation in HEMTs," in *2019 44th International Conference on Infrared, Millimeter, and Terahertz Waves (IRMMW-THz)*, vol. 2019-Sept. IEEE, 9 2019, pp. 1–1.

-
- [33] P. Fay, D. Jena, and P. Maki, *High-Frequency GaN Electronic Devices*, P. Fay, D. Jena, and P. Maki, Eds. Cham: Springer International Publishing, 2020.
- [34] A. P. Dmitriev, A. S. Furman, V. Y. Kachorovskii, G. G. Samsonidze, and G. G. Samsonidze, "Numerical study of the current instability in a two-dimensional electron fluid," *Physical Review B*, vol. 55, no. 16, pp. 10 319–10 325, 1997.
- [35] L.-P. Zhang and J.-K. Xue, "Plasma wave instability in a quantum field effect transistor with magnetic field effect," *Physics of Plasmas*, vol. 20, no. 8, p. 082118, 8 2013.

Design and implementation of an imaging XUV spectrometer

Patrícia Estrela¹

Abstract—In this work, we designed and implemented an XUV imaging spectrometer. We Kirkpatrick Baez as a condenser and imaging system, and a diffraction grating with spacing of $1 \mu\text{m}$ to spectrally separate the images. We obtained monochromatic images of a test target of Titanium from which we calculated the harmonics spectrum of two gas sources and the transmission of the target for both spectra.

I. INTRODUCTION

Typically, XUV images are resolved in space without any spectral information and spectral characteristics are usually acquired by a spectrometer without any space resolution. Even though these two data can be acquired simultaneously, for certain phenomena where for instance the transmission varies along the object or when there are different wavelengths created in certain regions of the object, this type of information is lost. Thus, it is useful to be able to acquire spectrally resolved images, especially in warm dense matter experiments where this type of phenomena are common.

II. IMAGING SPECTROMETER

A spectrometer is a device that is able to measure the spectral information of a light source by separating each wavelength in space [1]. Usually this separation is done by a diffraction grating. When radiation passes through this type of gratings each wavelength gets diffracted with a different angle θ given by:

$$d \sin \theta = m \lambda \quad (1)$$

where m defines the diffraction order, d is the diffraction grating spacing, and λ the wavelength.

This means that if we observe the radiation at a detector (in this case a CCD) at a given distance $l \gg d$ from the grating, each wavelength will be separated from the 0^{th} diffraction order by a distance D_{CCD} given by:

$$D_{\text{CCD}} = \frac{m \lambda}{d} \times l \quad (2)$$

From this relation, if the distance between the 0^{th} order and each diffracted wavelength is known, the corresponding wavelength can be determined. This is the basic working principle behind a typical spectrometer.

In order to add to this spectral information spatial resolution (*i.e.* imaging) we need to combine a spectrometer with an imaging setup [4]. In this way, the final output contains simultaneously different images for each wavelength. It is important to note that this method gives direct results only if

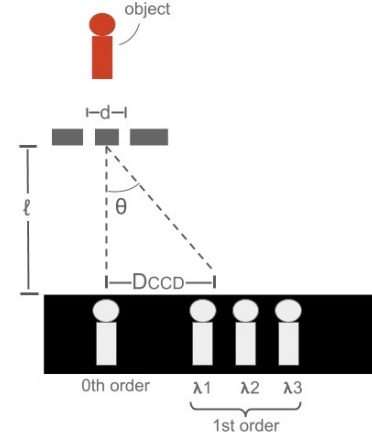


Fig. 1. Imaging spectrometer.

the light source spectrum is discrete, otherwise it wouldn't be possible to distinguish between images of continuous wavelengths and data deconvolution methods would be required.

Fig. 1. shows how an object is imaged in a CCD detector with spectral resolution, where we can see the separation between the 0^{th} order image and the images for each wavelength. The imaging setup is omitted in this figure for simplicity.

In order to preserve the bandwidth of the harmonics spectrum, the imaging system can be obtained from a pair of curved mirrors in Kirkpatrick-Baez geometry [2] [3]. In this geometry two concave mirrors are used at grazing incidence and placed orthogonal to each other, creating a point-like focus and thus can be used as a lens. Each concave mirror produces a tangential focus given by eq. (3).

$$f = \frac{R}{2} \sin \theta \quad (3)$$

R is the radius of curvature, θ is the grazing angle θ between the surface of the mirror and the beam.

The first mirror creates a line focus at a given plane and the second one compensates for the astigmatism and reduces the line-focus to a point. This system is very sensible to the alignment and can easily create astigmatism in the final image.

III. EXPERIMENTAL SETUP

Fig.2. and Fig.3. shows the experimental setup used in this work. The light source was obtained by high harmonic generation (HHG), a process where radiation is produced by the interaction of an infrared laser (IR) with a gas. We used

¹Patrícia Estrela is with Institute for Plasmas and Nuclear Fusion, Instituto Superior Técnico, University of Lisboa, Portugal.

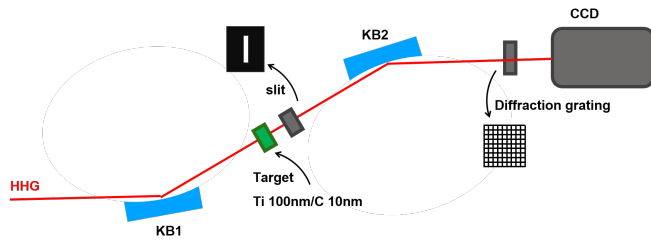


Fig. 2. Schematic of the experimental setup.

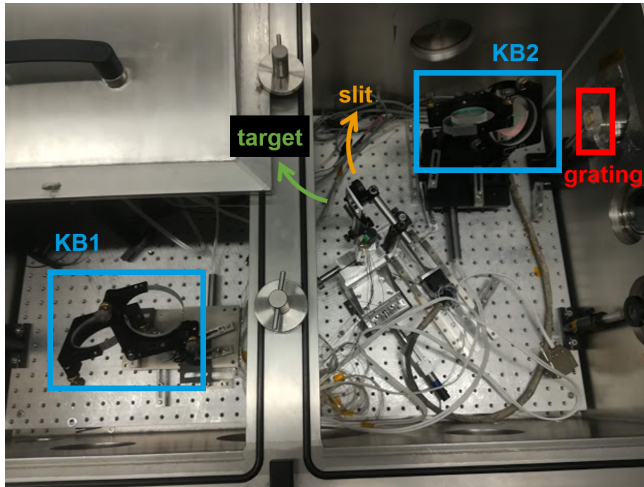


Fig. 3. Setup used in the experiment mounted inside the vacuum chamber.

a commercial Ti:Sapphire laser system, *Astrella* by Coherent Inc., to generate IR pulses at 800 nm of 35 fs duration at 10 Hz repetition rate. The IR was focused by a lens at a gas cell. We used two different gas sources (Argon and Xenon) to obtain two different spectra. The resulting harmonics (HHs) continued forward to a vacuum chamber while the remaining IR was blocked by two aluminum filters.

In order to increase the photon count on the CCD and improve the quality of the final image, the harmonics were focused on the target by a condenser which was a pair of KB mirrors (KB1).

The test target was a filter of titanium (Ti) with a mesh of $350 \mu\text{m}$, a thin layer of 100 nm of titanium (Ti) covered on each side with a thin layer of 10 nm of carbon (C). The target was placed between KB1 and KB2, close to the focus of KB1.

The imaging lens was obtained with a second pair of KB mirrors (KB2) placed between the target and the diffraction grating.

To obtain spectrally resolved images we placed a diffraction grating with spacing of $1 \mu\text{m}$ before the CCD. In order to separate the diffracted images on the CCD, we placed a slit of $200 \mu\text{m}$ in front of the target.

The most sensitive part of this setup was the alignment of the KB mirrors. For this alignment, we first started to align geometrically each pair outside of the vacuum chamber to guarantee that the angle between the incident and the reflected beam was correct. Afterwards, we placed both KB

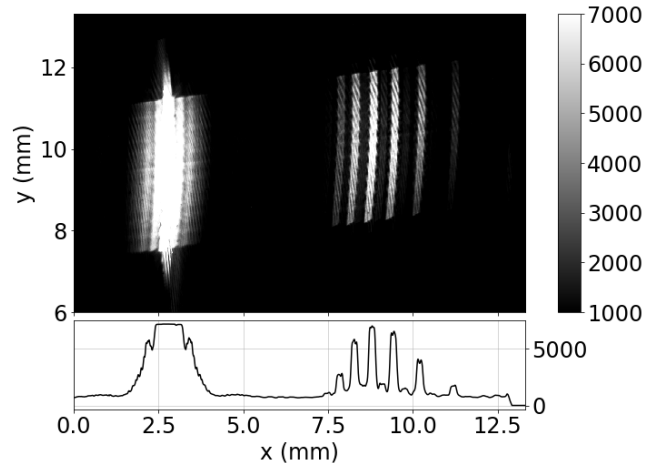


Fig. 4. Diffraction image of the slit obtained with HHG from Ar - 2s acquisition.

pairs inside the chamber and optimized their position by verifying the image formed at the CCD with a HeNe laser.

IV. RESULTS

We tested two different sources of HHs obtained from argon Ar (with maximum harmonic around 34 nm) and xenon Xe (with maximum harmonic around 47 nm). For each gas we obtained a diffraction image with and without the target. We calculate the transmission of each harmonic through the object by comparing the difference in transmitted intensity in both of these spectra.

Fig. 4. and Fig. 5. show the results obtained with Ar where we can observe that there is a difference in the spectrum with and without the object. Without the target we can distinguish the harmonics number 25, 23, 21, 19 and 17 with wavelengths of 32, 34.7, 38, 42.1, 47 nm, respectively. When the target was placed in front of the harmonics, only the harmonics 21, 19, and 17 were transmitted. Table I presents the expected and measured transmission values of each harmonic.

TABLE I
TRANSMISSION AR

Harmonic #	25	23	21	19	17	15
λ (nm)	32	34.7	38	42.1	47	53.3
expected (%)	0.004	0.39	5.96	7.75	4.07	1.71
measured (%)	-	-	6.8	6.68	1.66	-

Fig. 6. and Fig. 7. show the results obtained with Xe. Without the target the spectrum shows the harmonics 19, 17, 15 and 13 with wavelengths of 42, 47, 53.3 and 61.5 nm, respectively. When the target was placed in front of the beam only the 19, 17 and 15 harmonics were transmitted. Table II presents the expected and measured transmission values of each harmonic.

These results are justified by the transmission characteristics of each material in the target (Fig.8). The transmission of

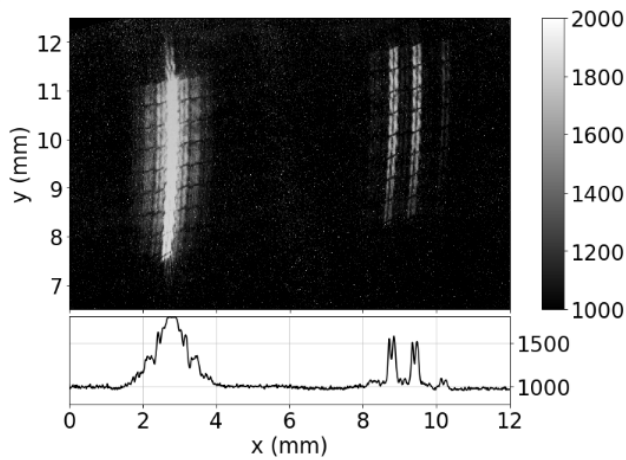


Fig. 5. Diffraction image of the slit with the target obtained with HHG from Ar - 30s acquisition.

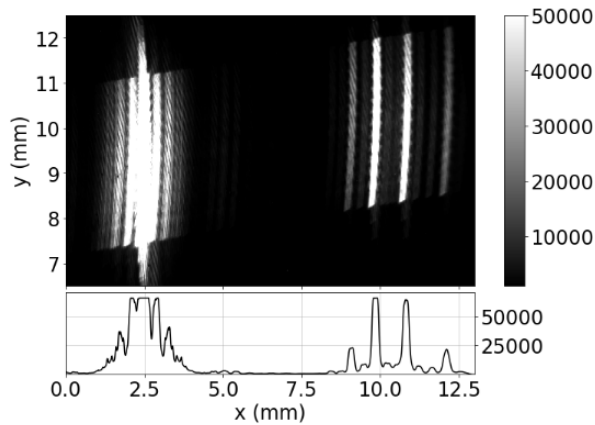


Fig. 6. Diffraction image of the slit obtained with HHG from Xe - 2s acquisition.

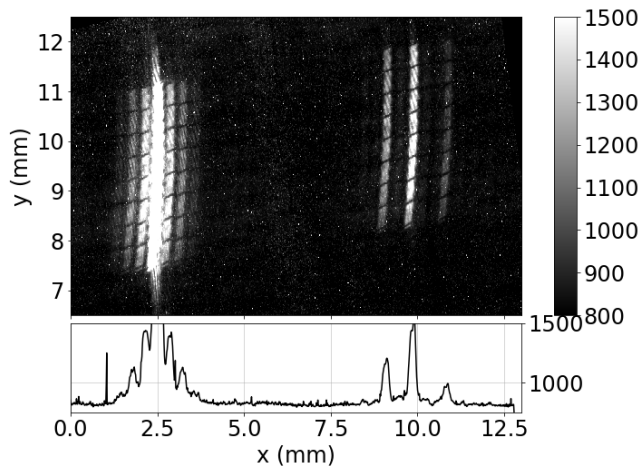


Fig. 7. Diffraction image of the slit with the target obtained with HHG from Xe- 20s acquisition.

the thin layer of carbon decreases with wavelength increase. In the case of the Titanium, there's a cutoff frequency below 40 nm, above this frequency the transmission starts to decline with wavelength again. The expected transmission values based on these two plots are presented in Table I and II.

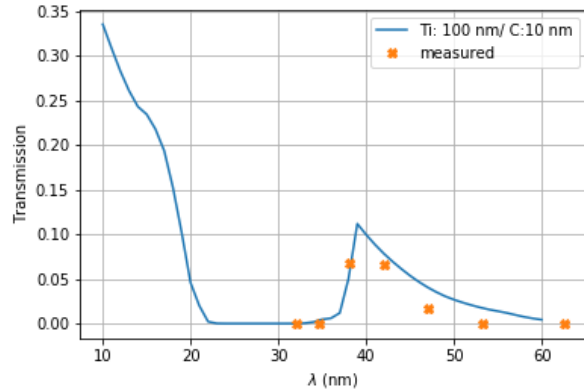


Fig. 8. Transmission of Ti (100 nm).

TABLE II
TRANSMISSION XE

Harmonic #	19	17	15	13
λ (nm)	42	47	53.3	61.5
expected (%)	7.75	4.07	1.71	0.29
measured (%)	2.04	1.16	0.38	-

V. CONCLUSION

We successfully setup an imaging spectrometer and obtained monochromatic images in the XUV range. We tested the transmission of a Titanium target for two different HHG spectra.

This imaging spectrometer can be used to spectrally image plasma phenomena. However the acquisition times used in this experiment are too long which result in a high number of laser shots. This can result in target damaging and thus we need to improve the number of counts/shot of this setup.

In the future, we can improve this number of counts/shot by optimizing the condenser since the image in the y direction is too wide and can be reduced without any loss of information. Another aspect of the setup that can be optimized is the magnification of the image. If the image is too magnified in the CCD there is a reduced number of photon counts and so by controlling this aspect we can also reduced the need for long exposure times.

REFERENCES

- [1] T. Kawachi, H. Suemitsu, K. Sawada, T. Fujimoto, T. Maehara, S. Yoshimura, T. Maekawa, and Y. Terumichi. In situ sensitivity calibration of an xuv spectrometer for plasma spectroscopy: Branching ratio method and collisional-radiative model. *Review of Scientific Instruments*, 66(2):1042–1046, 1995.
- [2] Paul Kirkpatrick and A. V. Baez. Formation of optical images by x-rays. *Journal of the Optical Society of America*, 38(9):766, Jan 1948.

-
- [3] L. A. Pickworth, J. Ayers, P. Bell, N. F. Brejnholt, J. G. Buscho, D. Bradley, T. Decker, S. Hau-Riege, J. Kilkenny, T. Mccarville, and et al. The national ignition facility modular kirkpatrick-baez microscope. *Review of Scientific Instruments*, 87(11), Oct 2016.
- [4] Martin Wünsche, Silvio Fuchs, Thomas Weber, Jan Nathanael, Johann J. Abel, Julius Reinhard, Felix Wiesner, Uwe Hübner, Slawomir J. Skruszewicz, Gerhard G. Paulus, and et al. A high resolution extreme ultraviolet spectrometer system optimized for harmonic spectroscopy and xuv beam analysis. *Review of Scientific Instruments*, 90(2):023108, 2019.

New acceleration regimes powered by lasers with arbitrary trajectories*

Bernardo Malaca¹

Abstract—Laser-plasma accelerators of electrons hold the record of maximum accelerating gradients. The quality and final energy of the electron beams have been improving recently. However, since research focuses on the same plasma waves that were proposed at the genesis of the field, the phase-space characteristics of relativistic particle beams have not changed. Recent advances in ultra-fast shaping of intense lasers motivate the exploration of arbitrary laser trajectories to probe new phase-space characteristics. In this work, we review methods to create arbitrary trajectories, detailing possible use on future laser-plasma acceleration, where this technique may improve electron energy by two orders of magnitude with respect to standard laser wakefield acceleration.

I. INTRODUCTION

In 1979, Tajima and Dawson [1] showed that lasers interacting with plasma can accelerate electrons to relativistic energies, due to the creation of an electrostatic plasma wave suited for that endeavour. This is now called Laser Wakefield Acceleration (LWFA). Over the next years, researchers found scaling laws for the 2D and 3D cases using computational models [2], [3] and produced multi-GeV quasi-monochromatic beams in the laboratory, attaining an acceleration gradient of up to 40 GV/m for 20 cm[4], [5]. The major improvement regarding the acceleration gradient of 200MV/m in traditional accelerators [6] – composed by radio-frequency cavities – means the cost and size of laser-powered accelerators could shrink by a factor of 1000.

In the majority of works that address acceleration, the laser pulse is assumed to be a perfect Gaussian. However, it is the laser that determines the shape of plasma waves [3], meaning that so far LWFA research explored only a subspace of the full range of the phenomenon.

In 1995, Rosen and Yariv [7] created arbitrary focal lines from computer-generated holograms. In 2007, Siviloglou and Christodoulides [8] proposed "accelerating Airy optical beams" – beams that propagated diffraction-free along a parabolic curve. The strict mathematical solution required infinite power and could not follow non-parabolic trajectories. In 2011, Greenfield et al [9] showed how to create Airy beams that can follow any one-dimensional curve in space.

Pursuing novel acceleration regimes requires the access to different degrees of freedom, which are unlocked by non-Gaussian pulses. For example, a laser with orbital angular momentum can create a plasma wave with angular momentum [10]. Vieira and colleagues showed this plasma wave originates a vortex electron beam where the electrons

have quantized angular velocities, even if they only interact classically with the laser [10].

In this paper, we review the recent advances in tailoring the laser phase and curvature to tailor the phase and curvature of a laser such that it follows arbitrary trajectories in space. This opens the possibility to luminal or superluminal propagation in a plasma overcoming the long standing limit of electron dephasing in the acceleration process.

II. GENERAL METHOD FOR THE CREATION OF ARBITRARY TRAJECTORIES FROM A PLANE WAVE IN 2D

The first step to understand how to create laser trajectories in 3D is to look at what happens at a smaller dimension using a plane wave with electric field $E = E_0 \cos(\omega t - kx)$. The wave propagates in the positive z direction, where at $z = 0$ passes through an infinitesimally thin phase mask. This phase mask has a phase distribution $\phi(x, z = 0)$, meaning that the electric field is now $E = E_0 \cos(\omega t - kx + \phi(x))$. Before the mask, every ray was travelling in the same \hat{z} direction, but now, at each point x_0 the light ray was deviated by an angle $\Theta = \delta\phi(x_0)/\delta x_0$ upon striking the mask. Within the Fresnel approximation, the evolution for the field (at $z > 0$) reads

$$u(x, z) = \int_{\text{mask}} \frac{1}{\sqrt{2\pi z}} e^{i\psi(x, z, x_0)} dx_0, \quad (1)$$

where $\psi(x, z, x_0) = k(x - x_0)^2/2z + k\phi(x_0)$, and k is the wave number.

Predicting the focus of $u(x, z)$ requires a careful look into the expression: the main contribution for $u(x, z)$ comes from points x_0^i where the oscillatory term $\exp(i\psi)$ halts, i.e. where $\psi'(x_0^i) = 0$. Selecting a trajectory means that for each $z > 0$, the maximum of $|u(x, z)|^2$ lays on top of the desired curve $f(z)$. Greenfield *et al* [9] showed that the solution of this problem is to make each light ray tangent to the desired f curve at the intersection point, as Figure 1 illustrates.

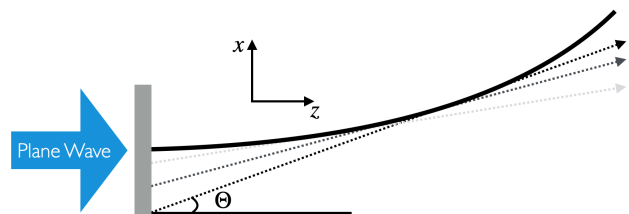


Fig. 1. Figure adapted from [9]. Desired focal trajectory in black. Three different light rays leave at the mask (in gray) tangent to the trajectory at the intersection point. The angle Θ is shown for a particular light ray. However, no ray coming from the mask could be tangent at the right-most point from the trajectory, no matter Θ .

*This work was supported by FCT

¹B. Malaca is with Institute for Plasmas and Nuclear Fusion, Instituto Superior Técnico, University of Lisbon, 1049-001 Lisbon, Portugal

This problem is explained via a set of two equations. Since each light ray is tangent it must have the same slope as f at the exact point where the light ray crosses f . The slope equation says that $\Theta = f'(z)$ whereas the crossing equation says $x = x_0 + z\Theta = f(z)$. The solution is not analytical can be calculated numerically for polynomial f . However, for the special case $f(z) = az^2$, we simply get $\Theta = \sqrt{4ax_0}$, which gives a phase mask with a phase distribution $\phi(x_0) = 2/3(4ax_0)^{3/2}$.

Greenfield *et al* created an experiment to observe focal spots that traveled along several polynomial trajectories and got focal lines that matched to theory. The size of the focus, measured with the full width at half maximum (FWHM), showed non-broadening peak-intensity even after 30 Rayleigh lengths. Figure 2 shows FWHM maintenance along with theoretical and experimental results for several curves.

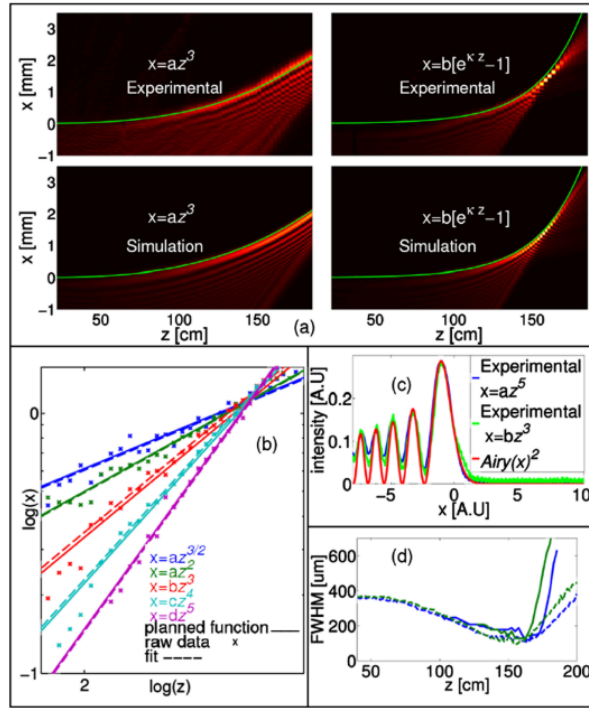


Fig. 2. Figure taken from [9]. (a) Comparisons between simulations and experiments for two particular curves, $x = az^3$ and $x = b[e^{kz} - 1]$; (b) Comparison between the planned function and the raw data for several polynomial functions; (c) Comparison between Experimental data and an Airy beam; (d) Experimental (whole lines) and simulated (dashed lines) full width at half maximum (FWHM) of beams which accelerate along the curves $x = az^5$ (blue [dark gray]) and $x = b[e^{kz} - 1]$ (green [medium gray]). The peak-intensity is nonbroadening, and even narrows up to 30 Rayleigh lengths of propagation, after which the beam abruptly starts to broaden

The function f must be convex – the light ray cannot cross f more than one time. Also, if the mask size is too small the coverage of f along z will be reduced, which can also be seen from Figure 1. It is also clear from figure 2 that there is a point in the trajectory where no light ray can be tangent. From that point forward the laser broadens abruptly. This method also ignores the time evolution of the field propagation, so we could not impose a certain velocity on the

focus, which requires both spatial and temporal information.

III. NON-BROADENING FOCAL TRAJECTORIES IN 3D – THE AXIPARABOLA

A. Construction

If we use a parabolic lens to focus a laser in a vacuum we will get a single focus and the laser will diffract (broaden) at its Rayleigh length scale $z_r = 0.5kw_0^2$, where w_0 is the beam waist at the narrowest point [12].

However, applications in LWFA could also benefit from a line focus, where the beam would focus along a line, keeping it at focus for the desired length. Smartsev *et al* [13] did so by using a reflective optics – the axiparabola. A reflective optics is defined by its sag function s , which represents the longitudinal distance from the mirror surface to an arbitrary reference point, as Figure 3 shows. In the case of a radially symmetric axiparabola $s = s(r)$.

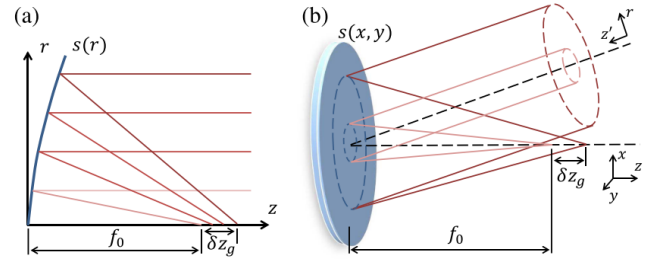


Fig. 3. Figure taken from [13]. The focal line goes from $z = f_0$ to $z = f_0 + \delta z_g$. (a) On-axis and (b) Off-axis case of light ray propagation (shades of red)

Rays that are parallel to the axis and strike the mirror at $z = s(r)$ are reflected according to the same principle described for 2D using Θ . The calculation of s is similar to that one of ϕ in the 2D case: the sag function $s(r)$ substitutes the phase distribution of the phase mask in 2D, meaning that a light ray striking the mirror at $z = s(r)$ is deflected at an angle $\Theta = ds/dr$. It is useful to note that this ray will cross the axis at $z = a(r)$ (the collection of the rays that cross axis at the same time is in fact a ring), according to

$$s(r) + \frac{r}{2} \left(\frac{1}{ds/dr} - ds/dr \right) = a(r), \quad (2)$$

Keeping constant intensity along the line requires

$$a(r) = f_0 + \delta z_g (r/R)^2, \quad (3)$$

as for each dr the amount of light each ring contains goes with r^2 (for symmetric axiparabolas each ring impinges on the mirror at the same time). Solving equation 2 for s gives the axiparabola profile. In the experimental setup designed by Smartsev, a laser reflected from the axiparabola and propagated through gas. Figure 5 shows that the laser peak intensity was maintained constant over 10 mm, which led to the formation of a plasma waveguide that could drive an intense laser pulse.

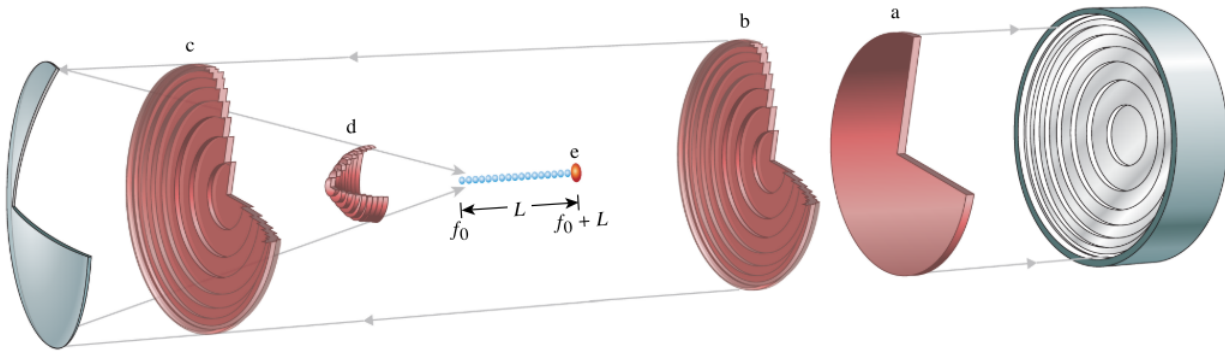


Fig. 4. Figure taken from [14]. Detailed explanation of direct laser wakefield acceleration (DLWFA): (a) laser is reflected on the echelon (b,c) laser with ring separation hits the axiparabola and (d) rings are then focused at different times and spaces so that (e) the interference pattern creates a focus travelling at c .

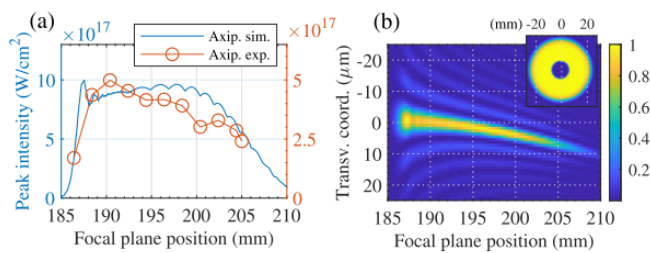


Fig. 5. Figure taken from [13]. (a) Peak intensity vs Focal plane position on a laser focused by an axiparabola: red circles are the experimental data and simulated data comes from a simulation using a 0.85J, 30 fs pulse. (b) Simulated time integrated Beam profile cross section as a function of the focal distance. Inset: Illumination profile used in the simulation

B. Axiparabola applied to laser wakefield acceleration

John Palastro *et al* [14] worked on a dephasingless laser wakefield acceleration (DLWFA), a method to shape a laser pulse that could increase the limits on the maximum energy limit attained in a single stage of a Laser wakefield accelerator. Dephasing is the process in which a normal Gaussian laser propagating through plasma travels at $\beta_l < 1$ and thus prevents particle acceleration if those particles have $\beta_p > \beta_l$ (outrunning the plasma wave). On DLWFA we then require to have a laser focus that travels at c , eliminating dephasing. They accomplished this by providing the ability to select velocity of the focus using another reflective optics in combination with the axiparabola – the echelon – that was able to induce a timeshift between different rings. Figure 4 details the full process. The rings with smaller radii are focused first and closer to the axiparabola, whereas the rings with larger radii are focused after and further away. Figure 6 illustrates the delay induced on the inner rings in relation to the outer rings. The depth difference between consecutive echelon levels is of the order of the wavelength λ , but the radial width is much larger, meaning no major optical aberration is induced.

The predictions for the energy gain are extremely positive, with some conditions allowing DLWFA to surpass standard LWFA by two orders of magnitude, as shown by Figure 7.

IV. CONCLUSIONS

Creating arbitrary focal trajectories with determined focal velocity would turn laser wakefield accelerators into a separate category from standard accelerators, due to the number of degrees of freedom that would be unlocked without extra cost.

The advances that are expected from focal trajectory manipulation show that this is a promising way to enhance laser wakefield acceleration. Acceleration of heavy ions could become a real possibility by using a smaller focal velocity. Being able to control the focal trajectory on 3D would allow further exploration in this field, such as the creation of bent ion channels and the dynamics of particles in these channels, along with the ensuing radiation. We reviewed in this work how a line focus can be used to enhance standard laser wakefield acceleration by up to two orders of magnitude, by increasing the useful length of an accelerator. This is by itself would be a great achievement, as laser wakefield accelerators are already better than conventional accelerators in terms of the electric field they impose on electrons. This would pave way to ultra compact accelerators that could substitute conventional accelerators in a multitude of fields. To the best of our knowledge, there is no information on how a plasma would react to even more unconventional light beams. Work in this direction is required to shed some light on the unknown.

REFERENCES

- [1] T. Tajima and J. M. Dawson, "Laser Electron Accelerator" *Phys. Rev. Letters*, 43:267–270, Jul 1979
- [2] W. Lu, C. Huang, M. Zhou, W. B. Mori, and T. Katsouleas, "Nonlinear Theory for Relativistic Plasma Wakefields in the Blowout Regime", *Phys. Rev. Lett.*, 96(16):165002, Apr 2006.
- [3] E. Esarey, C. B. Schroeder, and W. P. Leemans. "Physics of laser-driven plasma-based electron accelerators" *Rev. Mod. Phys.*, 81:1229–1285, Aug 2009.
- [4] W. P. Leemans *et al* "Multi-GeV Electron Beams from Capillary-Discharge-Guided Subpetawatt Laser Pulses in the Self-Trapping Regime", *Phys. Rev. Lett.*, 113(24):245002, Dec 2014.
- [5] A J Gonsalves *et al*, "Petawatt Laser Guiding and Electron Beam Acceleration to 8 GeV in a Laser-Heated Capillary Discharge Waveguide", *Phys. Rev. Lett.*, 122(8):84801, Feb 2019.
- [6] N. A. Solyak, "Gradient Limitations in Room Temperature and Superconducting Acceleration Structures", *AIP Conference Proceedings* 1086(1):365-372, 2009

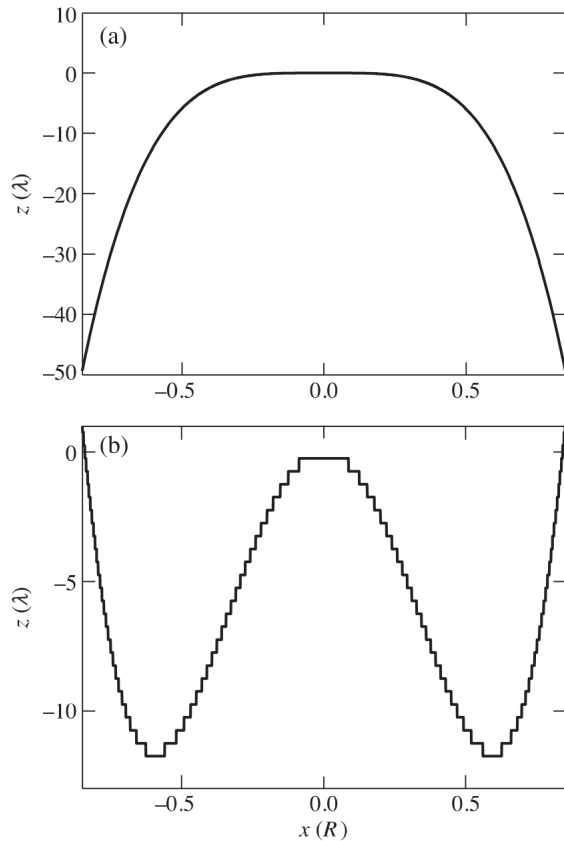


Fig. 6. Figure taken from [14]. (a) nonparabolic part of the axiparabola sag function (the parabolic term would represent a lens focusing the laser at f_0) (b) Echelon sag function. For visualization purposes, the laser would hit both these optics coming from $-\hat{z}$, which means that the inner rings are delayed with relation to the outer rings.

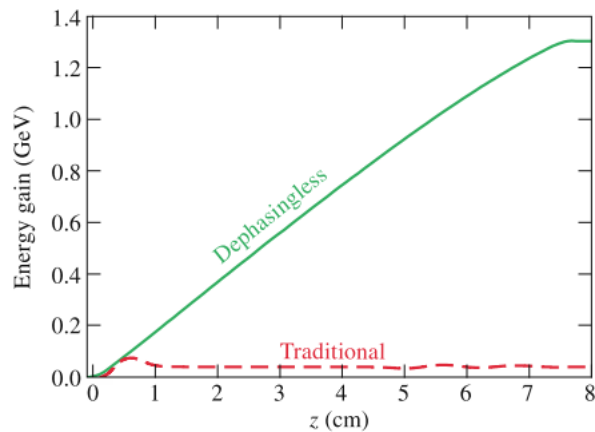


Fig. 7. Figure taken from [14]. The energy gain of electrons simulated in a DLWFA surpasses that in traditional LWFA. In the DLWFA, the electron gained 1.3 GeV over 16 dephasing lengths, while in the traditional LWFA, the electron eventually overtakes the wave and ends up with less than 0.1 GeV.

- [7] Joseph Rosen and Amnon Yariv, "Snake beam: a paraxial arbitrary focal line", *Opt. Lett.*, 20(20):2042-2044, Jun 1995
- [8] Georgios A. Siviloglou and Demetrios N. Christodoulides, "Accelerating finite energy Airy beams Georgios", *Opt. Lett.*, 32(8):979-981 Apr 2007
- [9] Elad Greenfield *et al*, "Accelerating light beams along arbitrary convex trajectories", *Physical Review Letters*, 106(21):1-4, 2011.
- [10] J Vieira *et al*, "Optical Control of the Topology of Laser-Plasma Accelerators", *Phys. Rev. Lett.*, 121(5):54801, Jul 2018.
- [11] M. Born, E. Wolf, "Principles of Optics", (Cambridge University Press, Cambridge 1999)
- [12] J. D. Jackson, "Classical Electrodynamics" (Wiley, New York 1975)
- [13] Slava Smartsev *et al*, "Axiparabola: a long-focal- depth, high-resolution mirror for broadband high-intensity lasers", *Optics Letters*, 44(14):3414, 2019.
- [14] J. P. Palastro, "Dephasingless Laser Wakefield Acceleration", *Phys. Rev. Lett.* 124, 134802, Mar 2020

Plasma Mirrors: a review

Miguel Pardal¹

Abstract—In this article, we review the main aspects and uses of plasma mirrors in the path for attosecond science and other applications. Here, we describe the basic functioning of a plasma mirror and its uses as a high-intensity optical component that can improve pulse contrast and filter unwanted pulse components. We also touch on the effect of using extreme intensity lasers and the non-linear and relativistic processes that come into play in those conditions. These processes can have some beneficial results like the generation of ultra-high harmonics from the incident laser pulse.

I. INTRODUCTION

A mirror is an optical component that comes in many shapes and sizes and, depending on the type, is used to reflect, redirect, or focus light in many experimental setups. The defining feature of a mirror is its ability to reflect light in a specular manner. *Specular reflection* is the reflection of a beam in which the angle of reflection is the same as the angle of incidence. Typically, mirrors are made by applying a reflective metal coating to a polished surface, although higher reflectivities are usually obtained with a dielectric coating [1]. The reflectivity of a mirror is the ratio between the incident and the reflected intensity of light.

The functioning of a mirror is very straightforward when using low to moderate intensity light ($I < 10^{13} \text{ Wcm}^{-2}$). However, when dealing with ultra-high intensity laser facilities, it is easy to come across ionizing beams of light that destroy conventional mirrors, creating a plasma at the interaction zone. Fortunately, this is usually a high-density plasma which can reflect light in the same way as a regular mirror [2], but unfortunately, under more extreme conditions ($I \gtrsim 10^{16} \text{ Wcm}^{-2}$) these plasma mirrors showcase non-linear [3] and relativistic behavior [4], [5], acting as an active optical element aside from specularly reflecting most of the incident light.

This paper will review the main aspects of plasma mirrors, their main uses, and possible applications. Section II discusses the process of creating a plasma mirror and its basic functioning. In Section III, we go through the most common uses of a plasma mirror as an optical component. Lastly, in Section IV, we review the non-linear and relativistic effects that occur when using higher intensities and discuss the possible ways in which these effects can be useful.

II. CREATION AND FUNCTIONING

A plasma mirror can be created by ionizing a flat target with a sufficiently intense laser pulse. When the target's surface atoms get hit by the laser, their electrons can be

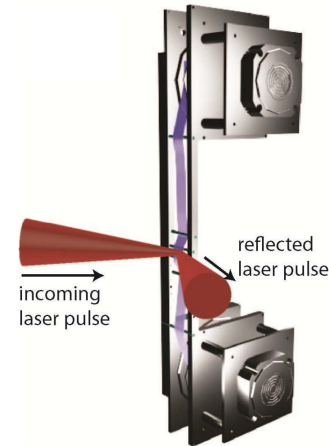


Fig. 1. A rolling tape mechanism for the replacement of the plasma mirror substrate. Taken from [9].

freed from the respective nucleus creating a plasma at the surface. The higher the intensity of the ionizing radiation, the larger is the number of free electrons, and consequently, the plasma density [6].

The light coming into the plasma mirror obeys the general laws for electromagnetic wave propagation in plasmas. This means that the laser gets reflected when the ionization is such that the plasma density surpasses the critical density, $n_c = m\varepsilon_0\omega_l^2/q_e^2$, for the given laser frequency, ω_l . Where q_e is the electron charge, m the electron mass, and ε_0 the vacuum dielectric constant. As an example, for a sub-100 fs laser pulse with 800 nm wavelength, the intensity required to create a critical density plasma mirror is about 10^{14} Wcm^{-2} .

With the creation of the plasma mirror, the target becomes damaged and can no longer be used as an optical component. Thus in order to ensure high repetition rates, a fresh target must be supplied at each shot. Thus movable target systems like rotating targets [7] or rolling tapes [8], [9] are usually employed. Figure 1 shows an example of the rotating VHS tape system: the incident laser pulse creates a plasma mirror on the smooth tape surface, damaging it in the process. Afterward, the motors move the tape to a new position, providing a fresh target for a new plasma mirror.

III. USES AS AN OPTICAL COMPONENT

The main use of a plasma mirror is to reflect high-intensity light. However, the fact that these components can be created from non-reflective surfaces has led to some exciting applications as a self-triggering optical switch [10].

¹Miguel Pardal is with Instituto de Plasma e Fusão Nuclear, Instituto Superior Técnico, Universidade de Lisboa, Lisbon, Portugal

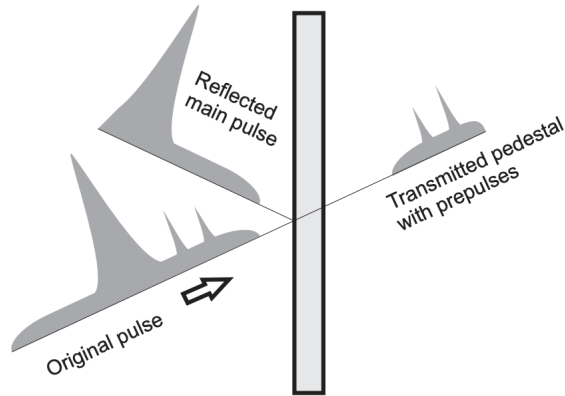


Fig. 2. Plasma mirror as a self triggering optical switch. The low intensity part of the pulse propagates through the plasma mirror substrate, while the main pulse is intense enough to ionize the surface and gets reflected off the plasma. Taken from [11].

An optical switch is a component that can switch an optical signal (*e.g.* a laser pulse) from one path to another. A plasma mirror created on a non-reflective object can act as an optical switch. Before the creation of the plasma mirror, the optical signal goes through the object. After the creation of the plasma mirror, the optical signal gets reflected onto a different path. We say that it is self-triggering because it is the optical signal itself that ionizes the surface, creating the plasma mirror, and consequently switching itself onto another path. Figure 2 shows an illustration of this process.

The fact that the intensity of the laser pulse is what triggers this switch means that this switch can filter the high-intensity radiation part of the laser pulse, effectively shortening it [12] and increasing its contrast [10], [13], [14].

This plasma mirror filtering effect can be beneficial when dealing with laser pulses that have long pedestals and lower intensity pre-pulses, which are commonly generated in the amplification processes [15], [16]. As Figure 3 shows, the plasma mirror improves the contrast of the laser pulse by four orders of magnitude and removes the pre-pulse present at $t = -10$ ps and front pedestal. This system also removes the pedestal behind the main pulse, not due to the optical switching, but rather due to the plasma dynamics that happen after the main pulse has passed, which leads to its diffuse reflection by the plasma mirrors.

Plasma mirrors are also a key component in some laser-plasma acceleration experiments [17], as Figure 4 shows. In Laser Wakefield Acceleration, particles inside a plasma experience high accelerating gradients created by a high-intensity laser pulse propagating in a plasma becoming an accelerated particle beam. These accelerating gradients are several orders of magnitude greater than the ones found in conventional accelerators, however, while propagating through the plasma, the laser loses energy and becomes out of phase with the particle beam, meaning that at some point the laser can no longer accelerate the particle beam. Multi-stage accelerators are a possible solution for this issue [18]

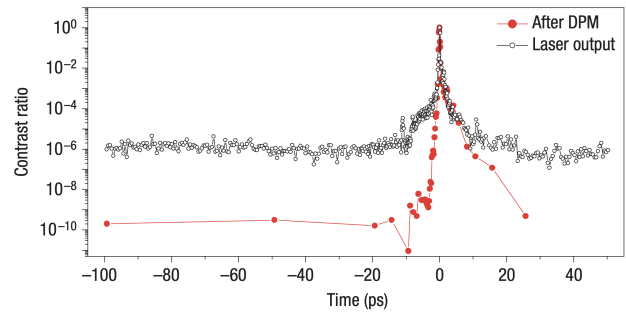


Fig. 3. Experimental data of the temporal profile of laser pulse before and after passing through a double plasma mirror set-up (negative times correspond to the front part of the beam). Taken from [16].

as they allow the particle beam to be accelerated by other laser pulses. For this scheme to work, we must guide the new laser pulse must into the particle beam path, which can be accomplished by using a mirror. In this aspect, a plasma mirror presents several advantages [8]:

- A plasma mirror can be created on extremely thin surfaces like VHS tape, this is important because the particle beam must travel through the mirror, and the thinner it is, the less energy the particle beam loses and the less it gets distorted
- A plasma mirror eliminates pre-pulses that come before the main pulse; this is important because having lower intensity pulses interacting with the plasma before the main pulse can be detrimental to the laser-plasma interaction.

In this way, plasma mirrors have found their place as high intensity optical components and are commonly used as optical switches at intensities from 10^{14} W cm^{-2} to 10^{16} W cm^{-2} , but as the laser intensity increases past 10^{16} W cm^{-2} , non-linear and relativistic effects start to take place and the plasma mirror can affect the reflected light in other ways.

IV. NON-LINEAR AND RELATIVISTIC EFFECTS

Experimental groups across the world have found evidence for the presence of harmonics of the incident laser in the reflected beam when using plasma mirrors, especially at high intensities ($I \gtrsim 10^{16}$ W cm^{-2}) [4], [5], [19], [20]. Coherent Wake Emission and Relativistic Oscillating mirror are the two major models that explain the appearance of higher harmonics in the reflected beam. They rely on non-linearities, and relativistic effects that arise when a plasma mirror is subjected to high-intensity laser fields.

A. Relativistic Oscillating Mirror

When the laser intensity exceeds $I \gtrsim 10^{18}$ W cm^{-2} , it generates a plasma mirror that oscillates at relativistic speeds, meaning that the light is effectively being reflected by a moving mirror. This induces a periodic Doppler shift in the reflected light that equates to a distortion of the original beam. As the period of this distortion is linked to the period

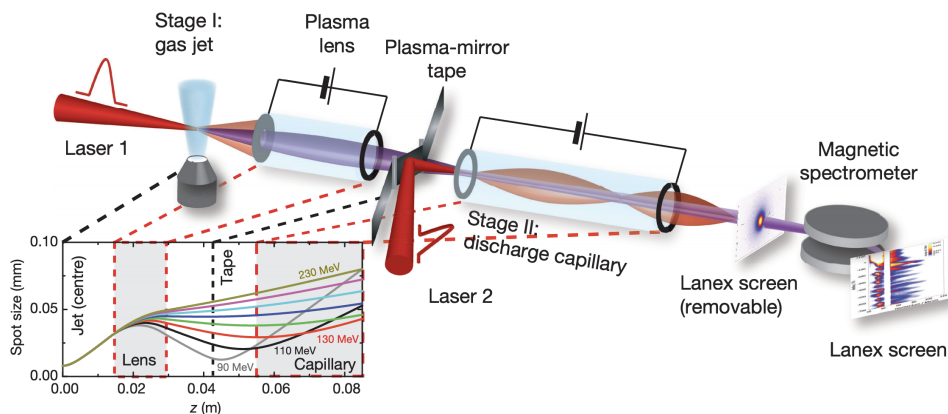


Fig. 4. Example of a double stage laser accelerator using a VHS tape substrate plasma mirror. *Laser 1* accelerates electrons in the gas jet of *Stage I*. These electrons are then focused by a *plasma lens* before going through the *plasma mirror*. The plasma mirror guides *Laser 2* into *Stage 2* where it further accelerates the electron beam. Taken from [17].

of the incident laser pulse, the resulting reflection contains high-order harmonics of the original beam [5].

The maximum possible order of the reflected harmonics depends on the velocity of oscillation of the plasma surface, which is connected to the intensity of the incident laser ($\omega_c \propto \gamma_m^3$, where ω_c is the maximum harmonic frequency and γ_m the Lorentz factor of the oscillating mirror) [21].

The presence of high order harmonics in the reflected beam can be a way to generate even shorter pulses of light, as a broader pulse in the frequency domain results in a sharper pulse in the temporal domain, if the harmonics are in the correct phase. Using this mechanism can potentially lead to the creation of attosecond (10^{-18} s) pulses of light [22]

B. Coherent wake emission

High harmonic generation can also occur for lower laser intensities ($I \lesssim 10^{18}$ W cm $^{-2}$), where the relativistic oscillating mirror mechanism is not efficient [16].

The so-called coherent wake emission process [23] can account for these observations. In this process, collective electron oscillations near the mirror surface emit light at multiples of the incident laser frequency. These density oscillations are driven by electrons that were pulled out of the plasma by the laser and pushed back by the plasma fields. This process can generate harmonics of the incident laser with frequencies up to the plasma frequency of the plasma mirror.

The kind of harmonics produced by this method are in many ways, different from the ones produced by the relativistic oscillating mirror [16]. Figure 5 shows a set of reflected spectra for different incident intensities. The authors of [16] show that for the lower intensity ($I = 3 \times 10^{18}$ W cm $^{-2}$), the maximum harmonic frequency corresponds to the plasma frequency of the plasma mirror (15th harmonic order), a clear trace of coherent wake emission. When the intensity of the incident beam is increased past the relativistic limit, the reflected pulse starts displaying more harmonics, with frequencies larger than the plasma frequency of the mirror, a clear trace of harmonics produced by a relativistic oscillating

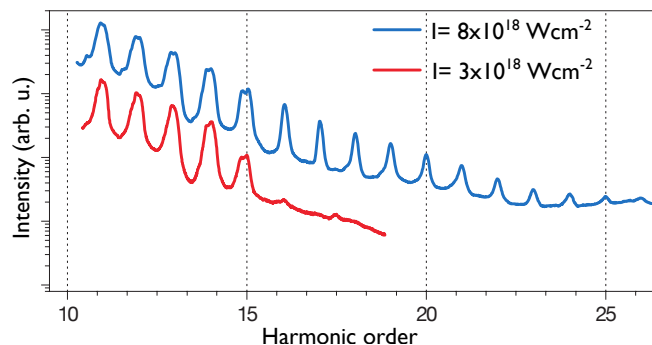


Fig. 5. Experimental data of spectra of light reflected by a plasma mirror in plastic (CH) and silica (SiO $_2$) at different intensities. Taken from [16].

mirror. Moreover, the authors also point out that the spectral width of the harmonics generated via the relativistic oscillating mirror is about half of the ones generated via coherent wake emission.

V. CONCLUSIONS

Plasma mirrors are a versatile high-intensity optical component. They can be used as an optical switch to filter low-intensity radiation, increase pulse contrast, or shorten pulse length.

Under more extreme conditions ($I \gtrsim 10^{16}$ W cm $^{-2}$), plasma dynamics start playing a more prominent role, and high harmonic generation takes place. Plasma mirrors are expected to be highly relevant in attosecond science as they allow the generation of high intensity, ultra-short, high-contrast laser pulses.

A significant drawback of laser-generated plasma mirrors is the plasma surface deformation caused by spatial variations of the extreme pressures (5 Gbar for $I \sim 10^{19}$ W cm $^{-2}$) exerted by ultra-intense lasers [24]. This is particularly relevant for the relativistic oscillating mirror model, as it usually assumes a flat oscillating surface. Usually, if the intensity variation around the focus is enough to induce a plasma surface curvature, the resulting deformation affects

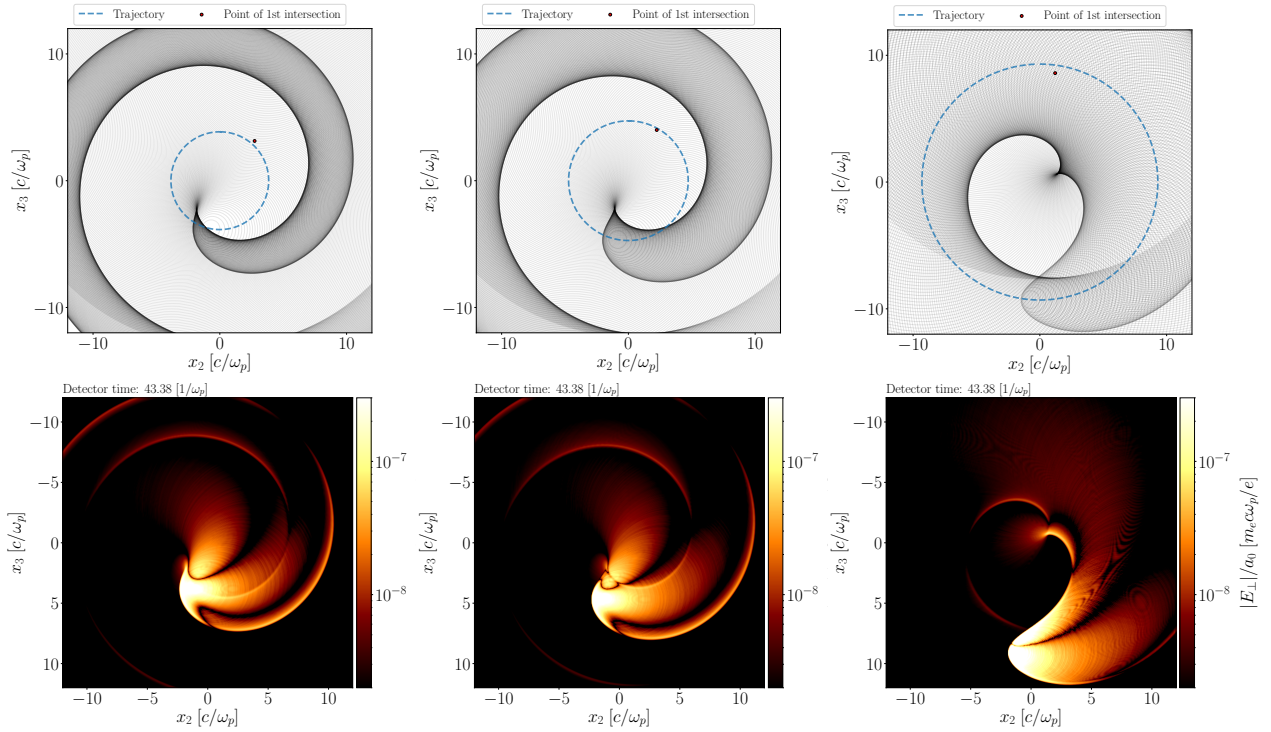


Fig. 6. Spatial profile of the radiation emitted by a spiral beam of particles decelerated due to the conservation of canonical momentum for 3 different spiral radii, r_{spir} . Comparison between simulations (bottom plots) and theoretical models (upper plots).

the spatial and spectral properties of the reflected beam and harmonics. Modeling the effect of this curvature and learning how to control it is, therefore, imperative.

In recent years, with the increasing interest in vortex light beam carrying orbital angular momentum [25], [26], some groups have identified plasma mirror high harmonic generation as a way to convert a circularly polarized laser pulse into a beam carrying orbital angular momentum [27], [28].

Moreover, plasma mirrors can be used to provide high amounts of acceleration to particle beams in ultra-short temporal scales. This is possible due to the conservation of canonical momentum \mathcal{P} .

$$\mathcal{P} = \mathbf{p} + e\mathbf{A} = \text{const} \quad (1)$$

where \mathbf{p} , e the electron charge and \mathbf{A} the E.M. vector potential. If the particle bunch co-propagating with a laser pulse collides with a plasma mirror, the laser pulse disappears, and as the vector potential associated with the laser pulse decreases, so must the particle's momentum. In this set up the deceleration decay length is directly tied to the plasma's skin depth, which can lead to the emission of ultra-short radiation pulses. Figure 6 shows preliminary results of simulations where a spiral beam of particles gets decelerated using this method, producing radiation.

All in all, the many uses of plasma mirrors as an optical component showcase the richness of laser-plasma interactions as well as their importance for modern science, as the maximum intensity of laser systems is pushed beyond its

limits.

REFERENCES

- [1] Joseph H. Apfel. Phase retardance of periodic multilayer mirrors. *Appl. Opt.*, 21(4):733–738, Feb 1982.
- [2] M. M. Murnane, H. C. Kapteyn, and R. W. Falcone. High-density plasmas produced by ultrafast laser pulses. *Phys. Rev. Lett.*, 62:155–158, Jan 1989.
- [3] Fabien Quere, C. Thauray, P. Monot, Sandrine Dobosz Dufrénoy, Ph Martin, J-P Geindre, and Patrick Audebert. Coherent wake emission of high-order harmonics from overdense plasmas. *Physical review letters*, 96:125004, 04 2006.
- [4] S. V. Bulanov, N. M. Naumova, and F. Pegoraro. Interaction of an ultrashort, relativistically strong laser pulse with an overdense plasma. *Physics of Plasmas*, 1(3):745–757, 1994.
- [5] R. Lichters, J. Meyer-ter-Vehn, and A. Pukhov. Short-pulse laser harmonics from oscillating plasma surfaces driven at relativistic intensity. *Physics of Plasmas*, 3(9):3425–3437, 1996.
- [6] G. Doumy, F. Quéré, O. Gobert, M. Perdrix, Ph. Martin, P. Audebert, J. C. Gauthier, J.-P. Geindre, and T. Wittmann. Complete characterization of a plasma mirror for the production of high-contrast ultraintense laser pulses. *Phys. Rev. E*, 69:026402, Feb 2004.
- [7] Yutaka Nomura, László Veisz, Karl Schmid, Tibor Wittmann, Johannes Wild, and Ferenc Krausz. Time-resolved reflectivity measurements on a plasma mirror with few-cycle laser pulses. *New Journal of Physics*, 9(1):9–9, jan 2007.
- [8] Brian Shaw, Sven Steinke, Jeroen Tilborg, and Wim Leemans. Reflectance characterization of tape-based plasma mirrors. *Physics of Plasmas*, 23:063118, 06 2016.
- [9] T. Sokollik, S. Shiraiishi, J. Osterhoff, E. Evans, A. J. Gonsalves, K. Nakamura, J. van Tilborg, C. Lin, C. Toth, and W. P. Leemans. Tape-drive based plasma mirror. *AIP Conference Proceedings*, 1299(1):233–237, 2010.
- [10] B. Dromey, S. Kar, M. Zepf, and P. Foster. The plasma mirror—a subpicosecond optical switch for ultrahigh power lasers. *Review of Scientific Instruments*, 75(3):645–649, 2004.
- [11] Tibor Wittmann. Complete characterization of plasma mirrors and development of a single-shot carrier-envelope phase meter. Master's thesis, University of Szeged, Szeged, 2009.

- [12] Claude Rolland and P. B. Corkum. Generation of 130-fsec midinfrared pulses. *J. Opt. Soc. Am. B*, 3(12):1625–1629, Dec 1986.
- [13] Henry C. Kapteyn, Margaret M. Murnane, Abraham Szoke, and Roger W. Falcone. Prepulse energy suppression for high-energy ultrashort pulses using self-induced plasma shuttering. *Opt. Lett.*, 16(7):490–492, Apr 1991.
- [14] Gilles Doumy, Fabien Quere, Olivier Gobert, Michel Perdrix, Ph Martin, Patrick Audebert, Jean-Claude Gauthier, J-P Geindre, and Tibor Wittmann. Complete characterization of a plasma mirror for the production of high-contrast ultraintense laser pulses. *Physical review. E, Statistical, nonlinear, and soft matter physics*, 69:026402, 03 2004.
- [15] Josef Cupal, Thomas Spinka, Emily Sistrunk, Bedrich Rus, and Constantin Haefner. Temporal pre-pulse generation in high-intensity CPA lasers from imperfect domain orientation in anisotropic crystals. In Pavel Bakule and Constantin L. Haefner, editors, *Short-pulse High-energy Lasers and Ultrafast Optical Technologies*, volume 11034, pages 24 – 33. International Society for Optics and Photonics, SPIE, 2019.
- [16] C. Thauray, F. Quéré, et al. Plasma mirrors for ultrahigh-intensity optics. *Nature Physics*, 3(6):424–429, Jun 2007.
- [17] S. Steinke, J. van Tilborg, et al. Multistage coupling of independent laser-plasma accelerators. *Nature*, 530(7589):190–193, Feb 2016.
- [18] Alexander Debus, Richard Pausch, Axel Huebl, Klaus Steiniger, René Widera, Thomas E. Cowan, Ulrich Schramm, and Michael Bussmann. Circumventing the dephasing and depletion limits of laser-wakefield acceleration. *Phys. Rev. X*, 9:031044, Sep 2019.
- [19] R. L. Carman, D. W. Forslund, and J. M. Kindel. Visible harmonic emission as a way of measuring profile steepening. *Phys. Rev. Lett.*, 46:29–32, Jan 1981.
- [20] B. Dromey, M. Zepf, et al. High harmonic generation in the relativistic limit. *Nature Physics*, 2(7):456–459, Jul 2006.
- [21] T. Baeva, S. Gordienko, and A. Pukhov. Theory of high-order harmonic generation in relativistic laser interaction with overdense plasma. *Phys. Rev. E*, 74:046404, Oct 2006.
- [22] George D Tsakiris, Klaus Eidmann, Jürgen Meyer ter Vehn, and Ferenc Krausz. Route to intense single attosecond pulses. *New Journal of Physics*, 8:19–19, jan 2006.
- [23] C Thauray and F Quéré. High-order harmonic and attosecond pulse generation on plasma mirrors: basic mechanisms. *Journal of Physics B: Atomic, Molecular and Optical Physics*, 43(21):213001, oct 2010.
- [24] H. Vincenti, S. Monchocé, S. Kahaly, G. Bonnaud, Ph. Martin, and F. Quéré. Optical properties of relativistic plasma mirrors. *Nature Communications*, 5(1):3403, Mar 2014.
- [25] L. Allen, M. W. Beijersbergen, R. J.C. Spreeuw, and J. P. Woerdman. Orbital angular momentum of light and the transformation of Laguerre-Gaussian laser modes. *Physical Review A*, 45(11):8185–8189, 1992.
- [26] J. T. Mendonça and J. Vieira. Donut wakefields generated by intense laser pulses with orbital angular momentum. *Physics of Plasmas*, 21(3):033107, 2014.
- [27] Genevieve Gariepy, Jonathan Leach, Kyung Taec Kim, T. J. Hammond, E. Frumker, Robert W. Boyd, and P. B. Corkum. Creating high-harmonic beams with controlled orbital angular momentum. *Physical Review Letters*, 113(15), oct 2014.
- [28] J. W. Wang, M. Zepf, and S. G. Rykovanov. Intense attosecond pulses carrying orbital angular momentum using laser plasma interactions. *Nature Communications*, 10(1):5554, Dec 2019.

Brief review of target normal sheath acceleration

Camilla Willim

Abstract—Target normal sheath acceleration (TNSA) driven by short intense laser pulses has attracted an impressive and steadily increasing effort. Motivations were found in the potential in applications such as proton radiography. Experiments have demonstrated the generation of multi-MeV proton and ion beams with unique properties such as ultrashort duration, high brilliance, and low emittance. An overview is given of the basic theory of TNSA and a three-dimensional particle-in-cell (PIC) simulation investigating the main observations from experiments.

I. INTRODUCTION

The observation of intense multi-MeV proton emission from solid targets irradiated at ultra-high intensities in three independent experiments in the year 2000 [1], [2], [3] corresponds to one of the major developments of "strong field science". The characteristics of the forward proton emission in the experiments, such as the short duration (ps), high degree of laminarity of the beam [4], the high number of protons ($10^{11} - 10^{13}$ protons in a single bunch), were attracting much interest both in fundamental research and in the possible applications. Moreover, the sources are compact, because the acceleration only occurs over a distance of about tens of microns.

Multi-MeV ions have a profile of energy deposition in dense matter which allows to deliver most of their energy at the end of their path, because the energy loss is dominated by Coulomb collisions for which the cross section grows with decreasing energy. Therefore protons and light ions are very suitable for highly localized energy deposition. Localized energy deposition finds its applications in ion beam cancer therapy, production of warm dense matter, "fast ignition" of inertial confinement fusion targets, and injectors for ion accelerators [5].

A high-intensity laser pulse directed on a solid target generates a plasma where strong electric fields occur due to a collective displacement of electrons. Such extreme electric fields accelerate ions up to an re-establishment of charge neutrality, after that ions and electrons move together in a ballistic way. The basic setup of the experiments is shown in Fig. 1 [5] which shows an artist's view. The protons were emitted as a moderately collimated beam, along the target normal direction, and detected at the opposite side of the irradiated solid target, also known as the rear side.

In 2001, Wilks et al. introduced a model called target normal sheath acceleration (TNSA) [7], where the longitudinally escaping hot electrons, generate a space-charge field at the rear side of the target, which accelerates the ions. The evidence that the protons were accelerated at the rear side has already been found one year earlier in

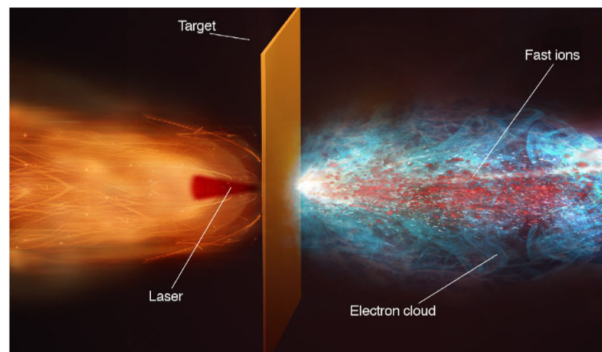


Fig. 1. Artist's view of a typical experiment on proton emission from solid targets irradiated by an intense laser pulse.

the experiment from Snavely et al. [3]. The acceleration mechanism TNSA, has reached a good level of reliability and robustness, and provides a framework for further developments, for example laser-controlled bunch control and post-acceleration. However, the before mentioned applications have stringent requirements on properties such as the energy per particle, the spectral distribution and the suitability for high-repetition rate operation [5], [6]. Those requirements cannot be achieved by TNSA yet and in order to meet the required parameters, multi-PW lasers and innovative developed targets need to be accessible. This issue has led to the proposal of alternative schemes, namely radiation pressure acceleration (RPA) or collisionless shock acceleration (CSA) whose investigation is still relatively preliminary compared to that for TNSA.

Because collective plasma dynamics is the basis of the outstanding properties of laser-accelerated ion bunches, its complex nonlinearity poses great challenges of control and modelling with respect to traditional approaches. Numerical simulations are used in order to understand the processes during and after the interaction better and to make predictions of possible outcomes for experimental setups. The so-called particle-in-cell (PIC) simulations are the most common approach in laser-plasma physics.

The purpose of this review article is to explain the basic theory of TNSA, followed by a discussion of one of the major three-dimensional PIC simulations.

II. BASIC THEORY OF TNSA

As mentioned in the introduction TNSA results from a charge separation produced by hot electrons escaping the target at the rear side. A cloud of relativistic electrons is expanding out of the target for several Debye lengths λ_D which creates an intense electric field mainly along the

normal to the surface. Therefore ions are accelerated from the rear side perpendicular to the surface and the ion beam is highly collimated. In the following the generation of hot electrons is discussed, followed by their effect on the ion acceleration at the rear side of the target.

A. Hot electrons

For TNSA a solid target is used, meaning that the electron density of the target n_e exceeds the critical density

$$n_{cr} = \frac{m_e \omega^2}{4\pi e^2}, \quad (1)$$

where ω is the laser frequency. When the critical density is smaller than the target density, i.e. $n_e > n_{cr}$, the laser pulse cannot penetrate and thus the pulse gets reflected. Although laser energy can get absorbed to a certain amount and heat up the plasma particles. When the laser intensity is extremely high, relativistic effects have to be encountered. Those relativistic effects make the target's refractive index nonlinear in the following way

$$n = \sqrt{1 - \frac{n_e}{\gamma n_{cr}}}, \quad (2)$$

where γ is the relativistic factor and given by

$$\gamma = \sqrt{1 + \langle \vec{a}^2 \rangle} = \sqrt{1 + a_0^2/2}, \quad (3)$$

with the normalized amplitude

$$a_0 = 0.85 \times \sqrt{\frac{I \lambda_{\mu m}^2}{10^{18} \text{Wcm}^{-2}}}, \quad (4)$$

which is related to the laser intensity and the wavelength in μm . When $n_e > n_{cr}$ but $\gamma n_{cr} > n_e$ we talk about relativistic self-induced transparency. The problem of laser penetration into plasma is not trivial because of the nonlinearity in the wave equation and the self-consistent modification of the plasma density as an effect of radiation pressure. Radiation pressure can be explained by the ponderomotive force, which on a heuristic level is the gradient of the time-averaged 'oscillation potential' of a laser field, the potential is expressing the quiver energy acquired by an oscillating electron. Physically spoken, the force tends to push electrons away from regions of locally higher intensity. As a consequence electrons are drifting away from the center of a focused gaussian laser pulse, both in transverse and propagation direction. The penetration of the laser pulse also depends on the target size, when the length is close to or smaller than the laser wavelength, i.e. $l \lesssim \lambda_0$, then the laser pulse can penetrate significantly.

For a solid target of several microns, i.e. $l \gg \lambda_0$ with a density $n_e \gg \gamma n_{cr}$ the laser pulse cannot penetrate crucially and the absorbed energy is transported to the deeper regions by hot electrons. Due to the use of laser intensities of $> 10^{18} \text{Wcm}^{-2}$ the hot electrons are relativistic and have an energy on the order of the cycle-averaged oscillation energy of the electric field in vacuum,

$$\varepsilon_p = m_e c^2 (\gamma - 1), \quad (5)$$

which is also called the ponderomotive energy [5].

B. Ion rear side acceleration

This section will provide a short overview about the rear side acceleration mechanism. Electrons from a solid foil target get accelerated by a short and intense laser pulse focused on the front surface of the target. Those electrons have a transverse but mainly longitudinal acceleration such that they cross the target and escape to the vacuum from the rear side. A charge unbalance is created and due to that a sheath electric field is generated normal to the target surface. This field both backholds electrons and accelerates the ions. We can relate the length of the sheath L_s and the temperature of the electrons T_h to the sheath field E_s in the following way [5]

$$eE_s \sim \frac{T_h}{L_s}. \quad (6)$$

In order to get an idea of the scalings, we discuss a simple example from [5]. Hence, we assume a laser irradiance of $I \lambda^2 = 10^{20} \text{Wcm}^{-2} \mu\text{m}^2$ and a fractional absorption of $\eta_h = 0.1$, leading to $T_h \approx 2.6 \text{MeV}$, $n_h \approx 8 \times 10^{20} \text{cm}^{-3}$, $L_s = \lambda_{Db} = 4.2 \times 10^{-5} \text{cm}$, and $E_s \sim 6 \times 10^{10} \text{Vcm}^{-1}$. The large electrostatic field backholds most of the electrons and accelerates the ions, such that they would acquire an energy of $\varepsilon_i \sim Z T_h$. The ion energy scales with \sqrt{I} if equation (6) holds.

III. PARTICLE-IN-CELL SIMULATIONS

The particle-in-cell (PIC) method is by far the most commonly method used to approach the non-linear and complex dynamics of laser-plasma interactions. Large-scale, one-dimensional to three-dimensional simulations running on supercomputers are a very effective support to design and understand laser-plasma acceleration experiments. The PIC method is mostly appropriate to describe collisionless interactions dynamics, because the method solves Maxwell-Vlasov system using a Lagrangian approach, with fields and currents allocated on a fixed grid and the phase space is represented by an ensemble of computational particles. Computationally such simulations are very expensive and it is challenging to find a simulation setup which can come close to experimental parameters.

This section gives a short overview of the simulation setup and the results which have been reported in 2001, in Pukhov's publication on one of the first large-scale three-dimensional simulations relevant to TNSA [8]. The group studied ion acceleration from a foil irradiated by a laser pulse at an intensity of 10^{19}Wcm^2 . This "model" simulation has been set in such a way that computational capabilities at that time were not exceeded. It is mentioned that the parameters might differ from usual experimental parameters. Nevertheless the group has been able to find evidence for the TNSA model introduced in the same year by Wilks [7] and is in agreement with observations in experiments.

Pukhov used the following setup for his simulation. He used a gaussian laser pulse in time and space with wavelength $\lambda_0 = 1 \mu\text{m}$, a pulse duration of 150fs , and a focal spot size of $5.6 \mu\text{m}$. The target is a overdense plasma layer of length $l = 12 \mu\text{m}$ and a density of $n = 16 n_{cr}$. In order

to simulate the preplasma which is present in laser-plasma interactions, he used a linear plasma ramp going from $0 - 16n_{cr}$ over a distance of $7.5\mu m$.

Two different acceleration mechanisms are discussed, ion acceleration at the front surface and at the rear surface. The ions are accelerated down the gradient of the laser intensity so that the angular directionality of accelerated ions at the front surface is defined by the particular pattern of the laser intensity distribution at the reflection point. The simulation showed a large ion emission cone of twice the expected size which is due to filamentary instability of the laser in the preplasma. These results are followed by the investigation of the accelerated ions from the rear surface which are extracted by the space charge potential of the hot electrons.

Due to the limited time in short laser pulse interaction, thermal equilibrium is not established and the electron distribution is two-temperature-like, where the lower temperature corresponds to the background electrons and the higher temperature corresponds to the electrons directly heated by the laser pulse. A comparison of the electron spatial distributions of the cold and hot electrons shows that the cold electrons stay within the original boundaries while the hot electrons escape into vacuum at the rear side and pull ions. Furthermore the hot electrons stay along the laser axis in the middle of the plasma even after the laser pulse has left for 100 laser periods. It is suggested that the reason for this is the self-generated magnetic fields which confine the electrons. A magnetic field gets frozen into the plasma and remains there. The azimuthal magnetic field is generated by the separation of forward and return currents and also beam filaments. Those electron beam filaments are generated by Weibel instability when the electrons are propagating through the plasma. The simulations confirm that a multichannel magnetic field structure is created in the target and guides the electrons in a collimated way through the plasma. When the electrons escape into the vacuum an azimuthal magnetic field of the order of 10 MG is generated in the nearest vicinity of the surface which collimates the electrons and influences the directionality of the plasma expansion. This feature is called fountain effect. The magnetic field is shown in Fig. 2 (a).

A sheath field which is accelerating the ions from the rear side and an azimuthal magnetic field which has the effect of collimation could be found. Due to those fields the strongest ion acceleration also happens exactly in the middle of the fountain effect. Such that the plasma expansion takes the form of a cone with the peak in the fountain center. The detected sheath field has a pronounced three-dimensional structure which accelerates ions with an angular distribution. It is shown in figure 2 (b). The recorded angular distributions from the simulation show annular structures with differing radii depending on the energy of the ions. Those ring structures have also been reported by an experimental group [9]. Pukhov suggests that the ring structures are caused by the 3D shape of the electrostatic field induced in the Debye sheath at the leading edge of the plasma expansion.

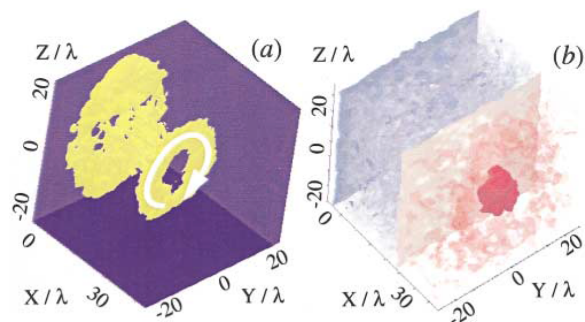


Fig. 2. 3D perspective views scaling with the laser wavelength λ . (a) Quasistatic magnetic field, the isosurface $|B| = 10$ MG is shown; the white arrow shows the field direction. (b) The accelerating electrostatic field $eE/mc\omega_0$, the isosurfaces have values: -0.05 (blue), 0.05 (red); the dark red blob in the middle marks the Debye sheath with the highest electric field $eE/mc\omega_0 = 0.1$.

IV. CONCLUSION

The basic principles of TNSA have been reviewed. Hot electrons are escaping a solid target irradiated by a high-intensity laser pulse and generate a strong sheath field which then accelerates ions at the rear side of the target. The generation of hot electrons and the generation of the sheath electric field have been discussed in order to understand the origin and the unique properties of the originated multi-MeV ion beam.

This field of research has attracted much interest and has shown unique potential both for innovative investigations and for applicative purposes. Theory and simulation have found a fruitful field, which poses original problems and suggests unexplored paths for reaching their solution. One of the first and major large-scale three-dimensional PIC-simulations is discussed, which has studied the TNSA acceleration mechanism.

Due to the need of meeting challenging ion beam properties for various applications the research area is very vital. Modern technology allows the use of other laser modes than the gaussian mode, as well as the development of new target structures. For example, high-intensity laser modes with orbital angular momentum are accessible nowadays and could lead to an enhancement of beam collimation or boost the accelerated ion energies. Due to the vitality of this research area, new setups will be investigated in the future.

REFERENCES

- [1] Clark, E. L., *et al.*, Phys. Rev. Lett. **84**, 670 (2000a).
- [2] A. Maksimchuk, *et al.*, Phys. Rev. Lett. **84**, 4108 (2000).
- [3] R. A. Snavely, *et al.*, Phys. Rev. Lett. **85**, 2945 (2000).
- [4] M. Borghesi, *et al.*, Phys. Rev. Lett. **92**, 055003 (2004).
- [5] A. Macchi, *et al.*, Rev. of Mod. Phys. **85.2**, 751 (2013).
- [6] Julien Fuchs, *et al.*, C. R. Physique **10** (2009)
- [7] Wilks, *et al.*, Phys. Plasmas **8**, 542 (2001).
- [8] A. Pukhov, *et al.*, Phys. Rev. Lett. **86**, 3562 (2001).
- [9] E. L. Clark, *et al.*, Phys. Rev. Lett. **84**, 670 (2000).

Kinetic Monte Carlo simulations of plasma chemistry*

T. C. Dias¹

Abstract—This work presents a Kinetic Monte Carlo algorithm to solve the gas-phase chemistry in plasmas, as a first effort to achieve an unified formulation of the electron and heavy-particle kinetics in low-temperature plasmas based on Monte Carlo techniques. The implemented algorithm is successfully validated from the comparison with the traditional deterministic description using rate-balance equations. Besides, we propose a modification in the standard stochastic method that strongly reduces the statistical fluctuations on the concentrations of the minor species.

I. INTRODUCTION

The strong non-equilibrium nature of low-temperature plasmas can efficiently enhance several chemical processes which are relevant for industry and other societal applications [1]. However, these systems are highly complex and they require a fundamental study from both experimental and modeling points of view.

Several plasma-chemistry models adopt a deterministic description to couple the solution of the electron Boltzmann equation to a system of rate-balance equations describing the heavy-species kinetics. The most common method to solve the electron Boltzmann equation relies on a low-anisotropy approximation, keeping only two terms in an expansion in Legendre polynomials:

$$f_e(\vec{v}_e) = \sum_{l=0}^{\infty} f_e^l(v_e) P_l(\cos\theta) \approx f_e^0(v_e) + f_e^1(v_e) \cos\theta, \quad (1)$$

which stands only for low reduced electric fields, $E/N \lesssim 100 \text{ Td} = 10^{-19} \text{ V m}^2$. In addition, there is a rather generalized use of “quasi-stationary” solutions to the electron Boltzmann equation, in which the Electron Energy Distribution Function (EEDF) is solved at each time-step for the instantaneous value of E/N . This strategy has been used successfully in a variety of discharges. However, it is not suitable for nanosecond pulsed discharges, subject of a growing interest in the last few years [2]. These discharges operate with very high reduced electric fields (of the order of 200 Td and above) and in the nanosecond time-scale. This is clearly a poor approximation due to the violation of the low-anisotropy assumption and because the time-scales of the changes in the EEDF can become comparable with the time-scale of variation of E/N .

The difficulties with the two-term and quasi-stationary approximations can be avoided with a self-consistent and unified formulation of the model based on Monte Carlo (MC)

techniques. The MC description of the electrons does not require an expansion in the velocity space and it includes from the very formulation the time-dependence of the electric field [3]. The simultaneous MC description of the heavy-species kinetics enables the inclusion of the time-dependent influence of different excited states of atomic and molecular species in the electron kinetics and vice-versa. In this work, we focus on the development of a stochastic MC method to study the heavy-species chemistry. In future works we will address the MC solution of the electron kinetics and the proper coupling with the chemical kinetics.

II. KINETIC MONTE CARLO

To the best of our knowledge, gas-phase chemistry in plasmas was never described with a MC approach, despite the success of the stochastic methods in describing relatively complex surface kinetics [4] and biochemical systems [5]. Here, we solve the heavy-species kinetics using the Kinetic Monte Carlo (KMC) algorithm developed by Gillespie [6] to simulate the temporal evolution of coupled chemical reactions. KMC simulations are exact, in the sense that they follow the time-evolution of one element of the statistical ensemble, simulated without any subjacent approximations. They provide answers to the questions “when and what”, determining the dynamics of the chemical species.

A. Algorithm

Consider a system constituted by N_s species that may undergo M reactions $\{R_1, \dots, R_M\}$, characterized by transition rates $\{a_1, \dots, a_M\}$. The stochastic description of the system is obtained with the following steps [6]:

- 1) Set the simulation time $t = 0$ and define the initial numbers of particles per species X_i ($i = 1, \dots, N_s$);
- 2) Calculate the transition rates a_v ($v = 1, \dots, M$) and the total transition rate $a_0 = \sum_v a_v$;
- 3) Generate two random numbers between 0 and 1: one for “when” (r_1) and another for “what” (r_2);
- 4) Calculate the time interval at which the next reaction will occur: $\tau = \frac{1}{a_0} \ln \frac{1}{r_1}$;
- 5) Find the reaction μ for which $\sum_{v=1}^{\mu-1} \frac{a_v}{a_0} < r_2 \leq \sum_{v=1}^{\mu} \frac{a_v}{a_0}$;
- 6) Update the numbers of particles X_i according to the selected reaction R_μ and set $t = t + \tau$;
- 7) If $t > t_{stop}$, stop the simulation; else, return to step 2.

Note that the time is obtained according to the probability density function $P_1(\tau) = a_0 \exp(-a_0\tau)$ and the reaction R_μ is selected according to $P_2(\mu) = a_\mu/a_0$. Moreover, the transition rates are calculated from the numbers of particles of the reactant species and the usual rate coefficients. More details can be found in [6].

*This work was performed under the APPLAuSE PhD program

¹T. C. Dias is with Instituto de Plasmas e Fusão Nuclear, Instituto Superior Técnico, Universidade de Lisboa, 1049-001 Lisboa, Portugal tiago.cunha.dias@tecnico.ulisboa.pt

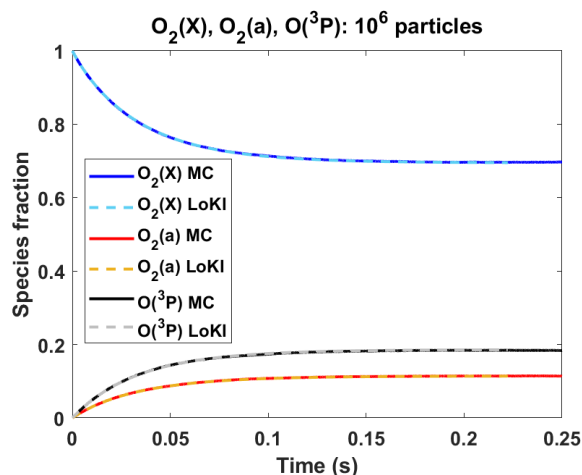


Fig. 1: Temporal evolution of $O_2(X)$, $O_2(a)$, $O(^3P)$, comparing KMC (10^6 particles) and LoKI.

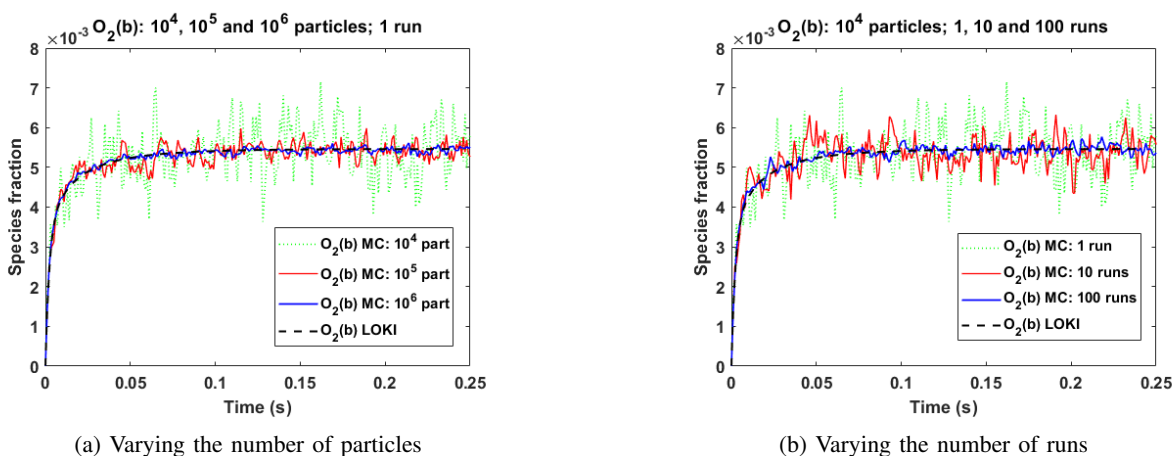


Fig. 2: Temporal evolution of $O_2(b)$, comparing KMC and LoKI.

B. Validation

The KMC algorithm used here was validated by Gillespie in [7] through a comparison of the MC results with deterministic calculations. However, this comparison was performed only for very simple chemical systems with few species and reactions. In this work, we use a realistic and much more complex system for the validation of the KMC algorithm: the heavy-species kinetics in an O_2 glow discharge. The simulation conditions used in the model are: $p = 1$ Torr, $T_g = 396$ K, $E/N = 48$ Td and $n_e = 6.5 \times 10^{15} \text{ m}^{-3}$ (corresponding to a current of 40 mA). The kinetic scheme is taken from Anušová *et al.* [9], considering 10 different species which interact through 63 reactions, and it describes relatively well the experimental results. The deterministic simulations are performed using the 0-D chemistry solver of the LisOn Kinetics (LoKI) tool suit [8], for the conditions and using the same kinetic scheme as in the KMC calculations.

Figure 1 shows the temporal evolution of the most abundant species in the discharge ($O_2(X)$, $O_2(a)$ and $O(^3P)$), comparing the KMC (with 10^6 particles) and LoKI simulations. The agreement is remarkable, which indicates that the methods are equivalent in this case. However, a substantial

factor for the smoothness of a MC simulation is the initial number of molecules in the system. To analyze this effect, we performed simulations with the same input conditions but with a different number of simulation particles. Figure 2a presents the time-evolution of the $O_2(b)$ fraction, where it can be observed that the more particles we put in the simulation, the smaller are the fluctuations of the results. Nonetheless, the simulation time increases linearly with the initial number of particles.

Another way to improve the accuracy of MC results is to average the results over several realizations of the system. In figure 2b, we find that, after averaging 100 runs with 10^4 particles, the statistical fluctuations around the average value of $O_2(b)$ are strongly reduced and comparable with those obtained with $10^4 \times 100 = 10^6$ particles. This approach is interesting from a computational point of view because the simulations may be launched at the same time in different computer cores. Since the simulation time is proportional to the initial number of particles, the total CPU time does not change, but the real time to obtain a given result decreases significantly. A similar conclusion was drawn in [4] regarding the application of KMC to describe surface kinetics.

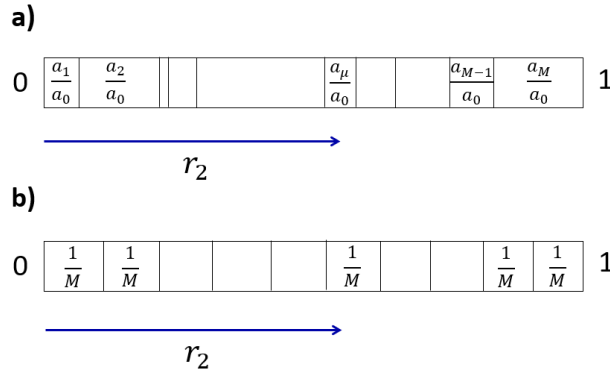
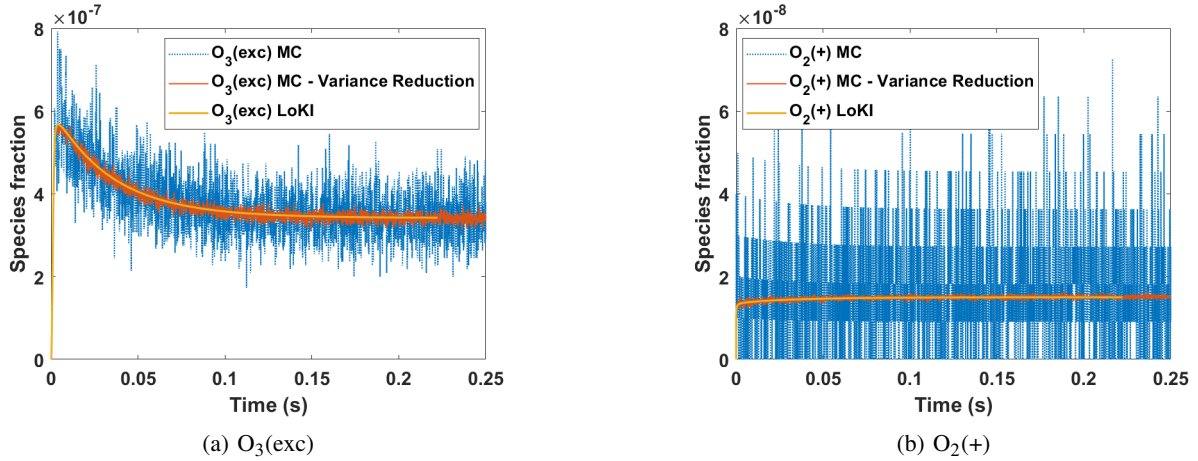


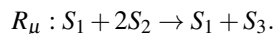
Fig. 3: Reaction selection: standard (a) and new (b) methods.

Fig. 4: Comparison between KMC (10^8 particles) and LoKI, using both standard and new methods.

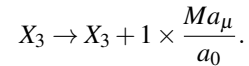
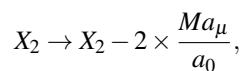
III. VARIANCE REDUCTION

Figure 2a reveals a major drawback of the standard KMC method: when we want to describe accurately the rare species in a discharge we need a large number of particles in the simulation, which may become very expensive in terms of CPU time. The (unphysical) statistical fluctuations on the calculation of the densities of the rare species are larger because the associated transition rates are much smaller and the correspondent reactions are rarely chosen.

In this work, we propose a variance reduction method, where the reaction selection is uniform (see figure 3): instead of having different intervals for each reaction v with length $L_v = a_v/a_0$, we consider a single interval for each reaction given by $L' = 1/M$, where M is the number of reactions. However, when a reaction μ is chosen, we have to correct its weight (importance) with the factor L_μ/L' . In this way, the importance of the reaction is corrected accordingly with the overestimation/underestimation made by homogenizing the reaction rates. For example, consider that the following reaction is chosen:



Then, the number of particles should be updated as follows:



Note that with this method we are no longer solving exactly the stochastic evolution of the system, as done in the standard KMC algorithm. Instead, we are acknowledging that there are some unphysical statistical fluctuations due to the fact that we use a small number of sample particles (e.g 10^8), compared to the real number of particles in the discharge (e.g. $\sim 10^{21}$). In this way, we give a small step closer to the deterministic approach, keeping the rest of the standard algorithm intact. If we are simulating a system which satisfies the thermodynamic limit, this method should be valid. If the number of particles of the real system is low, such that the statistical fluctuations are significant and physical, then we should use the standard KMC algorithm. However, in principle, most plasma-chemistry systems should agree with the thermodynamic limit due to the relatively high number of constitutive particles.

Figure 4 presents the fractions of two minority species (O₃(exc) and O₂⁺), comparing our approach with the standard one. Although the CPU time increases less than 10% relatively to the standard algorithm, we can reduce significantly the fluctuations using the new method.

IV. CONCLUSIONS

In this work, a Kinetic Monte Carlo algorithm to study the gas-phase chemistry was implemented, tested and compared with the traditional deterministic description. Moreover, to surpass the statistical fluctuations in the minority species, a reduction variance method was developed, consisting on the uniform choice of reactions.

In future works, we will address a different variance reduction technique, which allows to assign varying weights to the species. Finally, having an efficient and accurate KMC description of the gas-phase chemistry, we will move on to the MC solution of the electron kinetics and the proper coupling with the formulation presented in this work.

ACKNOWLEDGMENT

The author would like to thank Prof. Vasco Guerra for his fundamental support and several fruitful discussions.

REFERENCES

- [1] I. Adamovich *et al.*, “The 2017 Plasma Roadmap: Low temperature plasma science and technology”, *J. Phys. D: Appl. Phys.*, vol. 50, p. 323001, 2017.
- [2] R. Brandenburg *et al.*, “Fast pulsed discharges”, *Plasma Sources Sci. Technol.*, vol. 26, p. 020201, 2017.
- [3] S. Longo, “Monte Carlo simulation of charged species kinetics in weakly ionized gases”, *Plasma Sources Sci. Technol.*, vol. 15, p. S181, 2006.
- [4] V. Guerra and D. Marinov, “Dynamical Monte Carlo methods for plasma-surface reactions”, *Plasma Sources Sci. Technol.*, vol. 25, p. 045001, 2016.
- [5] A. Slepoy, A. P. Thompson and S. J. Plimpton, “A constant-time kinetic Monte Carlo algorithm for simulation of large biochemical reaction networks.”, *J. Chem. Phys.*, vol. 128, p. 205101, 2008.
- [6] D. Gillespie, “A general method for numerically simulating the stochastic time evolution of coupled chemical reactions”, *Journal of Computational Physics*, vol. 22, pp. 403-434, 1976.
- [7] D. Gillespie, “Exact Stochastic Simulation of Coupled Chemical Reactions”, *Journal of Computational Physics*, vol. 22, pp. 403-434, 1976.
- [8] A. Tejero-del-Caz *et al.*, “The LisbOn KInetics Boltzmann solver”, *Plasma Sources Sci. Technol.*, vol. 28, p. 043001, 2019.
- [9] A. Anušová *et al.*, “Kinetics of highly vibrationally excited O₂(X) molecules in inductively-coupled oxygen plasmas”, *Plasma Sources Sci. Technol.*, vol. 27, p. 045006, 2018.

ASDEX-Upgrade diagnostics for detachment characterization

Daniel Hachmeister¹

Abstract—In this paper, we summarize the current understanding of detachment - an essential phenomenon considered for the ITER design - by providing examples of diagnostic measurements routinely used to characterize detachment. We provide an overview of detachment's essentials, and we point the reader to the primary references in the field. We showcase four of the leading diagnostics employed by current machines to understand detachment, which is much needed to accurately model and predict detachment in future devices.

I. INTRODUCTION

Limiting the divertor power load to avoid damage is a significant challenge for ITER [1] and other future fusion devices [2]. For the tungsten tiles of the ITER divertor, the power load must stay below 10 MWm^{-2} during continuous operation. A detached divertor is necessary to achieve sufficient limiting of the divertor power load [3].

The first use of the term detachment referred to plasmas which formed an interaction boundary between the divertor target and the remaining plasma, effectively detaching the two [4]. During detachment, there is a decrease in energy, momentum, and ion flux parallel to the magnetic field lines from the midplane scrape-off-layer to the divertor target [5]. Detachment is possible due to the formation of a dense and cold plasma region above the divertor that shields it from the main plasma. Current devices achieve detachment by increasing plasma density via fueling (injection of fuel atoms) and seeding (injection of non-fuel atoms or impurities). Ions flowing to the divertor lose their energy through collisions with neutrals and other ions, and this energy dissipates as atomic line radiation [6]. Since most of the energy coming from the midplane scrape-off-layer is exhausted as radiation, the divertor target temperature can stay within safety limits.

Our current understanding is that energy dissipation occurs via three main channels, depending on the divertor temperature [5]. Initially, at 5-15 eV, energy dissipates as line radiation of low-Z impurity species that ionize and recombine continuously. Below 5 eV, ion-neutral elastic collisions and charge-exchange dominate over ionization. Finally, at 1 eV, plasma recombination dominates and results in a significant decrease in ion flux to the target.

Understanding the detachment mechanisms is necessary to model and predict divertor performance in future devices. However, some aspects of present-day observations still defy available simulation codes [7], e.g., the different detachment timing between the inner and outer divertor, as well as the asymmetries in particle flux [8], [9].

Characterizing detachment requires knowledge of the plasma parameters (density, pressure, and temperature) in the

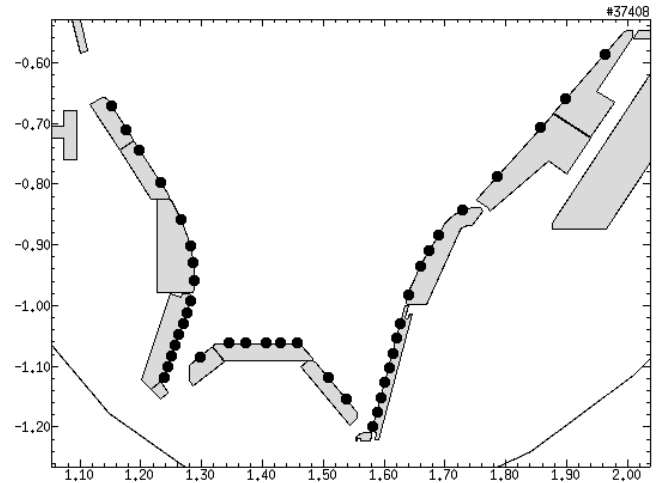


Fig. 1. Langmuir probes available in the AUG divertor.

scrape-off layer, the neighborhood of the divertor (divertor volume), and the divertor target plates. This paper describes four diagnostics available at ASDEX-Upgrade (AUG) used to characterize detachment and attain a better understanding of its governing physical processes.

II. DIAGNOSTICS

This paper covers four diagnostics and the plasma parameters they measure: Langmuir probes on the divertor surface that measure ion flux; divertor spectroscopy that measures average density on the divertor volume; fast diode bolometers that measure total radiated power spatially-resolved; plasma reflectometry that measures density as a function of the radius at the midplane.

A. Langmuir Probes

Figure 1 shows the Langmuir probes available at AUG. Each point in the figure represents a flush-mounted Langmuir probe that measures the ion flux (together with electron density and electron temperature). The onset of detachment is accompanied by a decrease in ion flux at the divertor compared to the expected scaling from the scrape-off-layer density [5].

Figure 2 shows a typical detachment scenario where the divertor ion flux increases and then decreases, a phenomenon called rollover. The dashed line represents the extrapolated ion flux without considering detachment, and the dots represent the total measured ion flux at the inner and outer divertor.

¹daniel.hachmeister@tecnico.ulisboa.pt

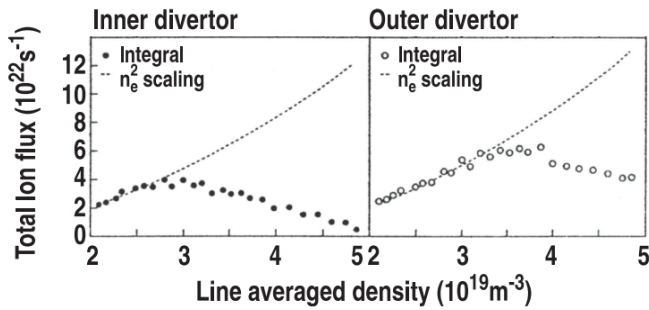


Fig. 2. Total ion flux across the divertor (integral) and expected scaling with the scrape-off-layer plasma density (n_e^2 scaling), adapted from [10].

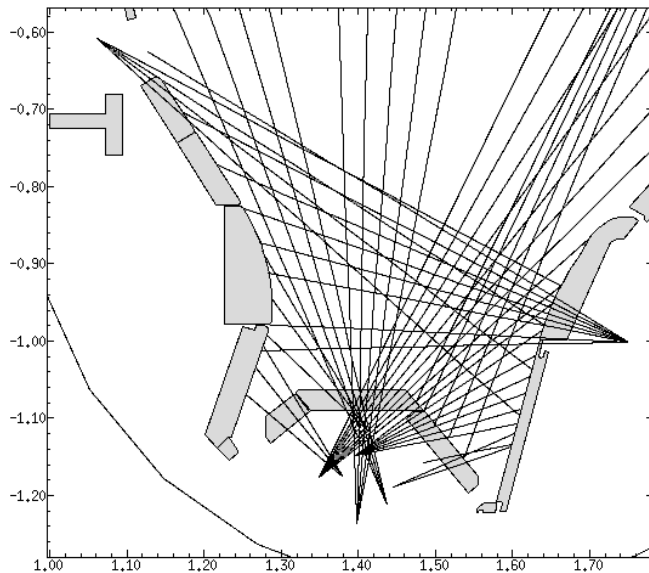


Fig. 3. Spectroscopy lines of sight (LOS) for measuring line-averaged electron density via stark broadening.

B. Divertor Spectroscopy

At AUG, spectrometers estimate the electron density n_e in the divertor volume by measuring the Stark broadening of the D_ϵ line [11]. Figure 3 shows the different lines of sight of the spectrometers. Although each line of sight measures a line-averaged density, crossing measurements from concurring lines yields a localized measurement of the electron density.

It is also possible to use spectroscopy to determine if the divertor plasma is dominated by ionization or recombination processes and hence infer the detachment stage. This is done by measuring the ratio of intensity between Balmer lines D_δ and D_ϵ [12]. As can be seen in figure 4, the ratio D_δ/D_ϵ quickly rises above 1.8 as the temperature drops below 1 eV, and recombination processes become dominant. Figure 4 also shows the similarities between ratios when the electron density differs by a hundredfold. The fact that this measurement is insensitive to electron density increases its robustness.

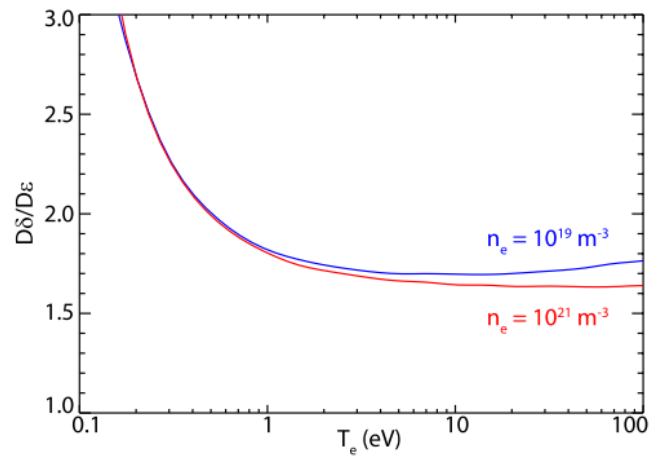


Fig. 4. Line intensity ratio D_δ/D_ϵ as a function of electron temperature for two different electron densities, adapted from [12].

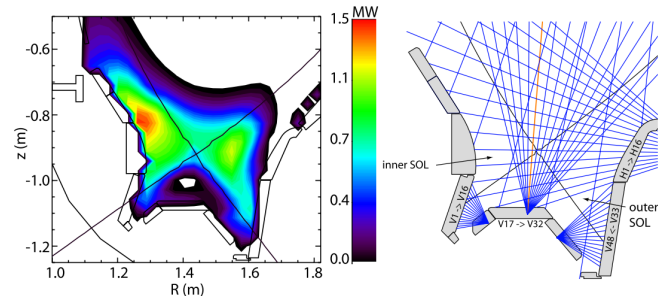


Fig. 5. Radiation distribution of the detached plasma (left), and lines of sight of the fast diode bolometers, adapted from [12].

C. Fast Diode Bolometers

Fast diode bolometers can measure the total radiation emission along certain lines of sight to determine a radiation distribution. At AUG, bolometers placed around the divertor measure the radiation distribution during detachment [12].

Figure 5 shows the radiation distribution of the detached plasma (left) and the lines of sight of the fast diode bolometers (right). This example shows the formation of a dense and highly radiative plasma near the HFS wall that is a prominent feature of a detached plasma [13].

D. Reflectometry

AUG has a reflectometry diagnostic that measures the radially dependent electron density from the high field side (HFS) and low field side (LFS) up to $6.45 \times 10^{19} \text{m}^{-3}$ [14].

Experimental observations have shown that the dense divertor plasma, responsible for detachment, can travel upstream to the HFS midplane, originating a high field side high-density front (HFSHD) at the midplane that might influence confinement [13].

The reflectometry diagnostic can measure the HFSHD, complementing the divertor diagnostics in characterizing detachment. As an example, figure 6 shows the radial density profiles before, during, and after detachment is completed. The density profile after complete detachment (red line)

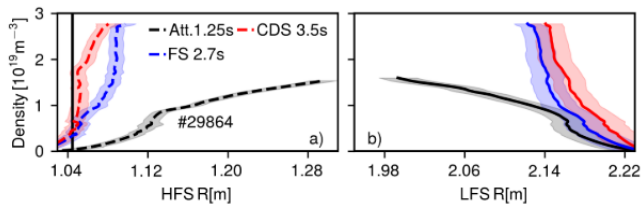


Fig. 6. Radial density profiles before (black), during (blue), and after (red) detachment is completed, adapted from [15].

exhibits an asymmetry between the LFS and the HFS. This observation is consistent with the formation of the HFSHD observed at the divertor [15].

III. CONCLUSIONS

The high exhausted power envisaged for future fusion reactors will require a detached plasma. This paper presents the main features of detachment as well as the diagnostic tools necessary to characterize it.

Modeling detachment is a difficult ongoing task due to (i) the multitude of phenomena associated with detachment; (ii) the fact that it encompasses both the divertor and the scrape-off-layer (iii) the asymmetries between high field side and low field side. These models can only be validated by extensive experimenting in current devices using the diagnostic methods here mentioned.

Langmuir probes can measure the decrease in ion flux to the divertor target due to detachment. Using spectroscopy, we can observe the chemical processes in the divertor volume that are the foundations of detachment. Fast diode bolometers measure the conversion of thermal energy to radiation during detachment. Using reflectometry, we can measure the influence of divertor detachment on the midplane density profiles both on the high and low field sides.

Current and future efforts in studying detachment based on a multi-diagnostic approach are sure to improve our understanding and capacity to accurately model detachment for the next-generation devices.

REFERENCES

- [1] "ITER - the way to new energy." [Online]. Available: <https://www.iter.org/>
- [2] "DEMO- EUROfusion." [Online]. Available: <https://www.eurofusion.org/programme/demo/>
- [3] R. A. Pitts *et al.*, "A full tungsten divertor for ITER: Physics issues and design status," *Journal of Nuclear Materials*, vol. 438, no. SUPPL, pp. S48–S56, 7 2013.
- [4] G. F. Matthews, "Plasma detachment from divertor targets and limiters," *Journal of Nuclear Materials*, vol. 220-222, pp. 104–116, 4 1995.
- [5] A. W. Leonard, "Plasma detachment in divertor tokamaks," *Plasma Physics and Controlled Fusion*, vol. 60, no. 4, p. 044001, 2 2018.
- [6] C. S. Pitcher and P. C. Stangeby, "Experimental divertor physics," pp. 779–930, 1997.
- [7] M. Wischmeier *et al.*, "Current understanding of divertor detachment: Experiments and modelling," *Journal of Nuclear Materials*, vol. 390-391, no. 1, pp. 250–254, 6 2009.
- [8] A. V. Chankin *et al.*, "Toroidal field reversal effects on divertor asymmetries in JET," *Control. Fusion*, vol. 38, pp. 1579–1592, 1996.
- [9] G. M. Staebler, "The critical point for the onset of divertor energy flux asymmetry in tokamaks," *Nuclear Fusion*, vol. 36, no. 11, pp. 1437–1453, 1996.

- [10] A. Loarte *et al.*, "Plasma detachment in JET Mark I divertor experiments," *Nuclear Fusion*, vol. 38, no. 3, p. 331, 1998.
- [11] S. Potzel, R. Dux, H. W. Muller, A. Scarabosio, M. Wischmeier, and ASDEX Upgrade team, "Electron density determination in the divertor volume of ASDEX Upgrade via Stark broadening of the Balmer lines," *Plasma Physics and Controlled Fusion*, vol. 56, 2014.
- [12] S. Potzel *et al.*, "A new experimental classification of divertor detachment in ASDEX Upgrade," *Nuclear Fusion*, vol. 54, no. 1, p. 013001, 11 2014.
- [13] —, "Formation of the high density front in the inner far SOL at ASDEX Upgrade and JET," *Journal of Nuclear Materials*, vol. 463, pp. 541–545, 7 2015.
- [14] A. Silva *et al.*, "Ultrafast broadband frequency modulation of a continuous wave reflectometry system to measure density profiles on ASDEX upgrade," *Review of Scientific Instruments*, vol. 67, no. 12, pp. 4138–4145, 12 1996. [Online]. Available: <http://aip.scitation.org/doi/10.1063/1.1147517>
- [15] L. Guimarães, "Poloidal asymmetries at the ASDEX Upgrade Tokamak," Ph.D. dissertation, Universidade de Lisboa, 2018.

Review of real-time control systems on JET

João Oliveira¹

Abstract—Research in controlled nuclear fusion appears to be most promising in magnetic confinement devices. Due to the nature of plasma instabilities these machines are dependent on real-time control systems to guarantee their safe operation. Currently the paradigm of operation of these machines is changing from a pulse based approach to continuous operation and as such the real-time control systems must adapt to this reality. In this paper we present a review of two real-time control systems of JET that are step forward towards continuous operation.

I. INTRODUCTION

The development of nuclear fusion for commercial power generation is based on the operation of experimental reactors around the world. These reactors use intense magnetic field to contain a plasma hot enough for nuclear fusion to occur inside the vessel of the reactor. Aside from the coils that generate the confinement magnetic field, a fusion experiment will also have a heating and current drive mechanism to heat the plasma and various diagnostics to monitor the plasma parameters. Due to the unstable nature of a fusion plasma these parameters must be monitored and controlled in real-time [1] and actuated upon by the other systems so that confinement is not suddenly lost, as such an event will put the containment vessel under heavy loads.

Due to their multiple control actuators, plasma diagnostics and large volume of experimental data fusion reactors need to use sophisticated control system and data acquisition (CODAC) systems. These systems naturally orient themselves towards a hierarchical architecture, with slower monitoring control systems at the top and faster, lower-lever systems at the bottom. The higher lever systems make general decisions about the state of the machine and in turn control the faster, lower-level systems that interact directly with the underlying instrumentation hardware.

The shift towards longer pulse times and eventual continuous operation in fusion experiments is placing new requirements on CODAC systems: they can no longer operate in a shot by shot paradigm where the experiment is done and then the data reviewed. This means that the systems must be capable to operate in streaming mode, where the experimental data is processed in real-time and eventually made available to the machine operator and the high level control systems so that they can make informed decisions on the operation of the experiment. The growth in the physical size and number of diagnostics implies that either the data transfer speeds must increase or developments in low-level data processing must happen.

Here we present brief review of some of the most relevant CODAC systems in current fusion experiments in JET.

Although it is not designed for continuous operation, the architecture of the control systems in JET is helpful in illustrating the evolution that is currently taking place.

II. REAL-TIME CONTROL SYSTEMS AT JET

The Joint European Torus is one of the largest tokamaks [2] in current operation [3]. Since its operation started its control systems went through multiple revisions and upgrades [4], [5]. Because of this the structure of its control system is rather heterogeneous with different subsystems aggregated together by a central supervisory machine (see Figure 1). We describe the control systems driving two recently upgraded subsystems, the gamma-ray diagnostics, and the plasma vertical stabilization system. It is important to note that although these systems do not operate in continuous mode currently the hardware they rely on can be used in this way and the basic architecture they use is well suited to continuous operation.

A. Gamma-ray diagnostics

JET has a number of gamma-ray diagnostics that are used to obtain information on the behavior of fast ions in the plasma. These diagnostics have similar control and data acquisition systems based on the advanced telecommunications computing architecture (ATCA) standard [6]. These systems are the Gamma-ray spectrometer, the Gamma Camera and the Gamma-ray spectrometer upgrade. The gamma-ray spectrometer and the gamma-ray spectrometer upgrade perform high-resolution gamma-ray spectroscopy at very high count rates [7], [8]. The Gamma-ray spectrometer support hardware consists of an ATCA host controller and four digitizer, all of these are installed on a ATCA 14 slot chassis (Figure 2)

The digitizer hardware consists of two field programmable gate arrays (FPGA) for real-time processing connected to two analog to digital inputs with a resolution of 14-bits capable of sampling rates of up to 400 million samples per second. The FPGA's implement a 1x PCI Express (256MB/s) link that is used to transfer data through the ATCA backplane. There are 2GB of DDR2 SDRAM on each of the digitizer boards that is used to store data [9].

The host controller consists of a PCIe switch connected to the ATCA backplane of the shelf and to a PC motherboard with an x86_64 CPU and 4GB of DDR3 SDRAM. The host controller runs the control and data acquisition software that is built upon the MARTe framework, a real-time application framework [10]. The software includes the CODAS interface library, which connects the diagnostic to CODAS, the MARTe GAM's that implement the real-time control algorithms and the MARTe IOGAM's that interface

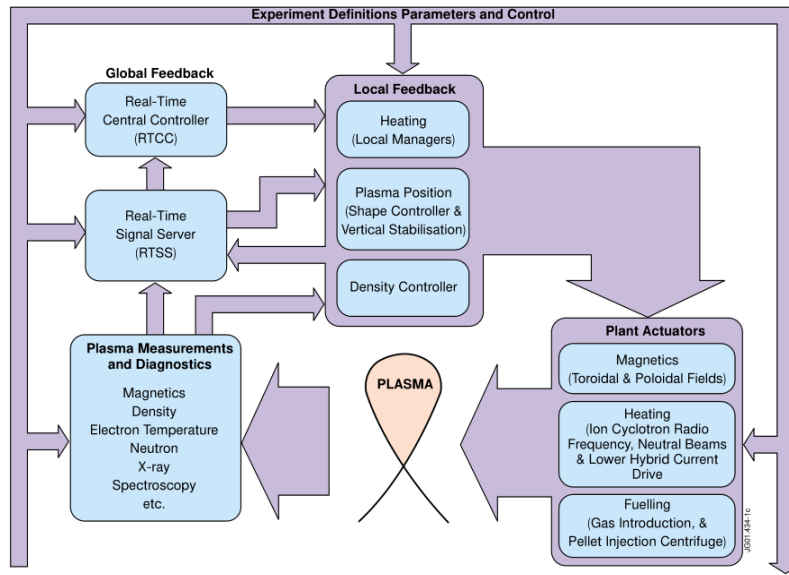


Fig. 1. Overview of real-time control at JET. Adapted from [4]

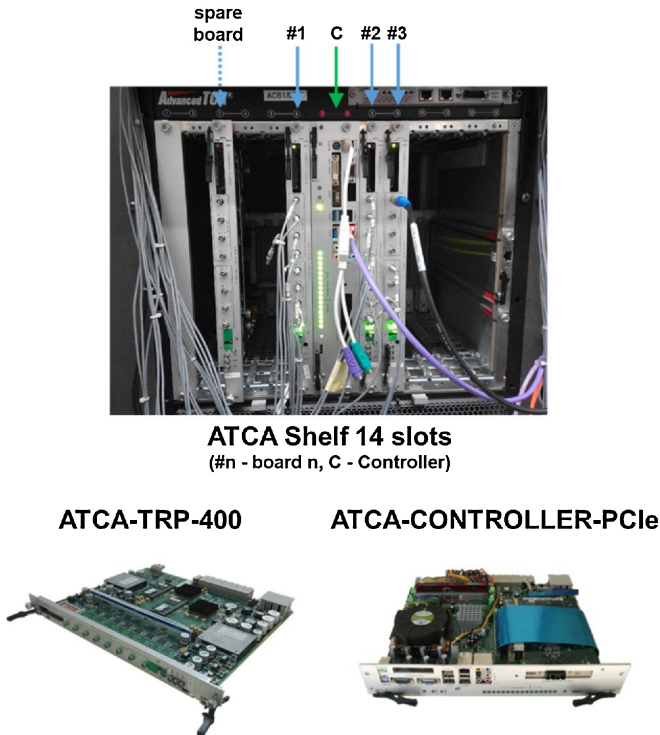


Fig. 2. Hardware environment for the Gamma-ray spectrometer at JET. Adapted from 2

of poloidal field coil that generate a radial magnetic field. The vertical stabilization control hardware is based on the ATCA standard. Two different communication fabrics are used simultaneously PCIe in a star mesh topology and Aurora in a full mesh topology (see Figure 3).

The hardware consists of a set of six ATCA-MIMO-ISOL [11] data acquisition and processing boards connected to the ATCA backplane together with a supervisory controller board based on a PC architecture. The data acquisition boards have a modular design and support up to 32 isolated 18-bit 2MSPS ADC channels and 8 isolated DAC channels. At the core of the board is a Xilinx Virtex 4 that is responsible for collecting the data from the analog inputs, perform data processing and transfer to the supervisory controller.

The supervisory control board consists is built around a x86_64 PC system architecture combined with a PCIe bridge connected to the ATCA backplane. This board runs the vertical stabilization real-time control software [12] that was developed using the MARTE framework. In the context of MARTE the control software is a collection of GAMs that work together to execute the control algorithm. The data from the data acquisition board is read by the input GAM and is passed along to the other GAMs that form the control loop until the actuation signal is passed to the interface to the DACs.

III. CONCLUSIONS

Both of the systems reviewed featured an architecture based on the ATCA standard that consists of multiple digitizer boards connected to a supervisory unit through the ATCA backplane. This architecture allows for a logical flow of data by using fast, massively parallel programmable logic devices, at a low level to process a large volume of data in real-time, reducing its volume. Because off this this architecture is well suited continuous operation. Although

MARTE with the digitizer modules and thus receive data from the modules, and are also responsible for their configuration at the beginning of the pulse.

B. Vertical stabilization system

The vertical stabilization system in JET controls the vertical instability inherent to the elongated shape of the plasma used in JET [1]. This is accomplished by actuating a set

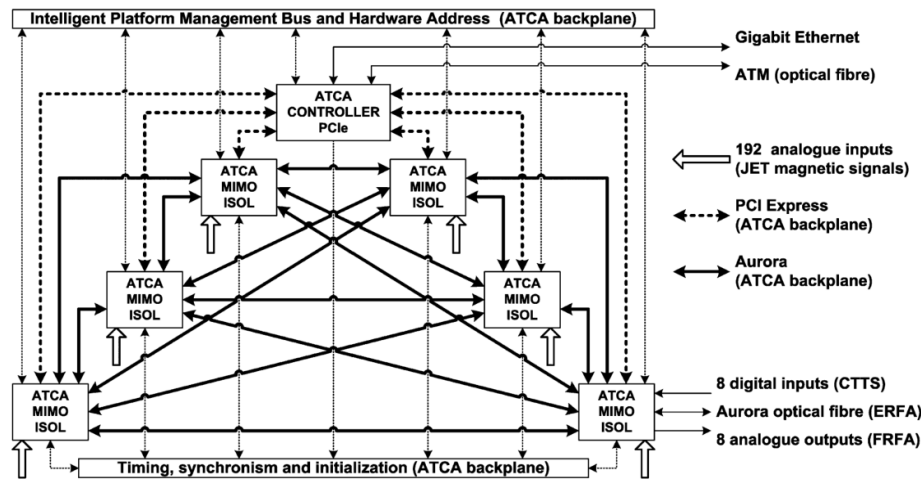


Fig. 3. Vertical stabilization architecture. Adapted from [11]

the systems reviewed do not operate in this mode their fundamental design logic is a stepping stone towards the this new paradigm of operation. Furthermore recent developments in the technology of interconnection protocols and programmable logic can enhance the capabilities of real-time control systems. to process a large volume of data in real-time, reducing its volume. Because off this this architecture is well suited continuous operation. Although the systems reviewed do not operate in this mode their fundamental design logic is a stepping stone towards the this new paradigm of operation. Furthermore recent developments in the technology of interconnection protocols and programmable logic can enhance the capabilities of real-time control systems.

REFERENCES

- [1] R. Albanese, E. Coccorese, and G. Rubinacci, "Plasma modelling for the control of vertical instabilities in tokamaks," *Nuclear Fusion*, vol. 29, no. 6, p. 1013, 1989.
- [2] J. Wesson and D. J. Campbell, *Tokamaks*. Oxford university press, 2011, vol. 149.
- [3] E. Laszynska, P. Batistoni, A. Cufar, Z. Ghani, S. Jednorog, L. Packer, S. Popovichev *et al.*, "In-vessel calibration of jet neutron detectors: Comparison of methods of neutron emission rate determination," *Fusion Engineering and Design*, vol. 146, pp. 1661–1664, 2019.
- [4] A. Goodyear, S. Dorling, and R. Felton, *The evolution of real-time control systems at JET*. European Fusion Development Agreement. Project, 2001.
- [5] J. Krom, "The evolution of control and data acquisition at jet," *Fusion engineering and design*, vol. 43, no. 3-4, pp. 265–273, 1999.
- [6] B. Santos, A. Fernandes, R. Pereira, A. Neto, J. Bielecki, T. Craciunescu, J. Figueiredo, V. Kiptily, A. Murari, M. Nocente *et al.*, "Control and data acquisition software upgrade for jet gamma-ray diagnostics," *Fusion Engineering and Design*, vol. 128, pp. 117–121, 2018.
- [7] M. Curuia, T. Craciunescu, S. Soare, V. Zoita, V. Braic, D. Croft, A. Fernandes, J. Figueiredo, V. Goloborod'ko, G. Gorini *et al.*, "Upgrade of the tangential gamma-ray spectrometer beam-line for jet dt experiments," *Fusion Engineering and Design*, vol. 123, pp. 749–753, 2017.
- [8] A. M. Fernandes, R. C. Pereira, A. Neto, D. F. Valcárcel, D. Alves, J. Sousa, B. B. Carvalho, V. Kiptily, B. Syme, P. Blanchard *et al.*, "Real-time processing system for the jet hard x-ray and gamma-ray profile monitor enhancement," *IEEE Transactions on Nuclear Science*, vol. 61, no. 3, pp. 1209–1215, 2014.
- [9] R. Pereira, J. Sousa, A. Fernandes, F. Patrício, B. Carvalho, A. Neto, C. Varandas, G. Gorini, M. Tardocchi, D. Gin *et al.*, "Atca data acquisition system for gamma-ray spectrometry," *Fusion engineering and design*, vol. 83, no. 2-3, pp. 341–345, 2008.
- [10] A. C. Neto, F. Sartori, F. Piccolo, R. Vitelli, G. De Tommasi, L. Zabeo, A. Barbalace, H. Fernandes, D. F. Valcárcel, and A. J. Batista, "Marte: A multiplatform real-time framework," *IEEE Transactions on Nuclear Science*, vol. 57, no. 2, pp. 479–486, 2010.
- [11] A. J. N. Batista, A. Neto, M. Correia, A. M. Fernandes, B. B. Carvalho, J. C. Fortunato, J. Sousa, C. A. Varandas, F. Sartori, and M. Jennison, "Atca control system hardware for the plasma vertical stabilization in the jet tokamak," *IEEE Transactions on Nuclear Science*, vol. 57, no. 2, pp. 583–588, 2010.
- [12] T. Bellizio, G. De Tommasi, P. McCullen, A. C. Neto, F. Piccolo, F. Sartori, R. Vitelli, and L. Zabeo, "The software architecture of the new vertical-stabilization system for the jet tokamak," *IEEE transactions on plasma science*, vol. 38, no. 9, pp. 2465–2473, 2010.

Assessment of mobile radiation detector's systems considering different scenarios

Luís Marques¹, Alberto Vale² and Pedro Vaz³

Abstract—This study presents a review of research advancements in the field of gamma and neutron measurements for Mobile Detection Systems considering aerial and ground-based platforms. For this purpose three scenarios will be described and analysed: reactor accidents; Illicit traffic of nuclear and radiological materials; and Naturally Occurring Radioactive Materials (NORM). For gamma detection and spectroscopy normally are used the NaI (Tl), CsI (Tl), LaBr₃ [Ce] and BGO scintillators, as well as the semiconductor Cadmium Zinc Telluride (CZT). For scenarios which involves the detection of Special Nuclear Materials (SNM) is also used neutron detectors. Relevant techniques for field measurement of gammas and neutrons are also discussed. This comprehensive analysis intends to help understand the detection system performance requirements for each scenario and challenges that may occur in operational environments, therefore optimizing the overall system sensitivity and reducing survey times.

Index Terms—Mobile Detection Systems, unmanned systems, nuclear radiation, Emergency scenarios.

essential aspect of interdiction of radiological threats for national security purposes [2].

To the best of our knowledge, a comprehensive review article covering the gamma and neutron detection systems coupled to ground and aerial based platforms with regard to different scenarios has not been published in the literature.

Due to the increasing importance of nuclear technology, whether from an industrial or military point of view, it is essential to standardize in situ detection methods that allow mapping and monitoring of contaminated areas.

This article intends to study the performance of different detection systems coupled to mobile vehicles and the factors that influence the detection, localization, quantification and identification of radioactive sources considering the specific scenario and operational environment.

I. INTRODUCTION

This paper considers the salient developments in mobile detection systems for ground and aerial-based platforms from the era after the Fukushima Daiichi Nuclear Power Plant (FDNPP) accident (2011). Additionally, technological gaps and the directions for future research are also highlighted.

It is known the significant potential for the use of mobile detection systems, in particular remote control vehicles, however no attempt to standardise sampling and measurement methods using these types of vehicles has been done so far. Doing so would simplify the use of remote control vehicles in an emergency scenario and would thus be very valuable for example in Critical Infrastructure Protection (CIP) [1].

Despite the similarity between hand-held and vehicle mounted detectors, there are significant differences as: the size of the detection system which must be reduced significantly to fit these dynamic platforms; the resolution; the sensitivity; and the robustness.

A wide range of gamma detectors have been investigated regarding their possible application. Since plutonium, a material used for nuclear weapons, is a significant source of fission neutrons, the detection of this particle is also an

II. BACKGROUND

There are several radiation measurement and sampling scenarios that are too risky to be performed by humans. Some of the scenarios foreseen are accidents in nuclear reactors (radioactive plumes and deposition of radioactive material in the ground - fallout), the illicit release of radioactive material (e.g. radiological dispersion devices), the location of radioactive material outside the regulatory control (MORC), as well as the survey and monitoring of contaminated areas in the long term [1]. Examples of significant incidents at nuclear installations include Three Mile Island, USA (1979), Chernobyl, Ukraine (1986), and Fukushima, Japan (2011). Incidents involving significant radiation exposures to radioactive sources include exposure of people to abandoned sources (New Delhi, India, 2010), occupational accidents (Chile, 2005), and medical over-exposures (Epinal, France, 2004). Concerns regarding potential malicious uses of radioactive and nuclear materials have increased with the heightened awareness of international terrorism.

In a release and / or contamination by radioactive material it is important to determine the radioisotopes present and the intensity of radiation in a given area. The field of radiation monitoring can fall into two distinct categories: - The location, identification and quantification of a radioactive source; - The mapping of a contaminated area, in which it is intended to represent the distribution of the radiation field over a pre-defined area. It allows quantifying areas of risk, becoming a tool to support the decisions of governments and authorities, for example with regard to the protection of a task force or a population against a nuclear accident [3].

¹L. Marques is with the Centro de Investigação da Academia da Força Aérea, Academia da Força Aérea, Sintra, 2715-311 Pêro Pinheiro, Portugal lumarques@academiafa.edu.pt

²A. Vale is with Instituto de Plasmas e Fusão Nuclear, Instituto Superior Técnico, Lisboa, 1049-001 Lisboa, Portugal avale@ipfn.tecnico.ulisboa.pt

³P. Vaz is with the Department of Radiation Protection, Centro de Ciências e Tecnologias Nucleares, Instituto Superior Técnico, Loures, 2695-066 Bobadela, Portugal pedrovaz@ctn.ist.utl.pt

III. MOBILE RADIATION MONITORING SYSTEMS

Mobile Monitoring systems includes: hand-held equipment's; manned and unmanned ground-based vehicles (UGV); and manned and unmanned aerial vehicles (UAV)). The systems are capable of performing in situ measurements as well as collecting various kinds of samples. Environmental and surroundings-related factors affect both the behaviour of releases and performing of proper radiation measurements, for example Weather conditions (e.g. influence of atmospheric conditions on dispersion of release plumes) and Urban vs. rural surroundings. An emergency monitoring authority must be prepared to cope with a variety of radiation situations with different source terms, time behaviour and exposure paths, therefore it is important to know in advance all characteristics of a particular measuring system [4].

A. Ground-based platforms

Ground-based mobile detection methods, such as handheld detectors and those installed in a manned vehicle, despite providing good spatial resolution, require significant data collection time for large areas, which cannot exceed safe exposure limits. These methods are unsuitable for making measurements in inaccessible places (e.g. forests, cultivation fields, roofs, etc.), or as a first form of research in response to a scenario where the intensity of radiation is unknown.

B. Air-based platforms

Aerial-based mobile detection can be divided in Fixed Wing, rotatory wing and Vertical take-off and Landing (VTOL).

Manned Aircraft are limited to minimum safety altitudes, which for airplanes is normally around 150 m. Also the corresponding ground speed (typically 90 km/h) is a limitation factor for ground contamination measurements given low spatial resolutions. However there is possibility of using helicopters which also posses the problem of radiation limits for the crew due to high doses.

UAVs major technological acceleration within the field has been evident since the incident at the FDNPP in March 2011 [3]. Missions where fixed-wing unmanned air vehicles are superior compared to other unmanned platforms include radioactive plume tracking, sampling of airborne radioactive material, fallout mapping of large areas and searching of unshielding point sources, e.g. Material Out of Regulatory Control (MORC), both stationary and moving, from large areas [2]. Rotary wing may present different configurations, e.g. with a main and tail rotors (conventional helicopter) or having three or more rotors (multi-rotors). Despite their advantage of hovering they have relatively shorter operating endurance/range and payload capabilities [2]. VTOL Aircrafts that have this capability can hover and also have the tradicional plane design for speed and range.

IV. RADIATION DETECTION SYSTEMS

Since they are uncharged particles and can travel further, neutron and gamma-ray detection can lead to the identification of radiological sources in general, including nuclear materials.

Gamma ray detectors can be broadly categorized into three classes: gas-filled detector; scintillation detector and solid-state detector [6]. As an example of a Gas-filled detector there is the general purpose Geiger-Muller (GM). Due to their spectrometry capability in this study it will only be described with some detail the scintillators and semiconductors.

Table I presents a resume of materials available for use as scintillator detectors and some critical characteristics that serve as a measure of the effectiveness of a radiation detector like the: energy resolution; counting efficiency; and inherent dead time [5].

TABLE I
RESUME OF THE SCINTILLATORS MAIN CHARACTERISTICS

Scintillator	$\Delta E/E$	Light yield (Photons/MeV)	Decay time (μ s)	Pulse Shape Disc.	Physicochemical properties
NaI(Tl)	7.5–8.5%	38000	0.23		Hygroscopic
CsI(Tl)	7.2%	65000	0.68 (64%)	Good	Less Hygrosc. and Brittle
LaBr3[Ce]	2.8%				Inferior Hygroscopic (NaI/CsI)
BGO	13.6%	8200	0.3		Good mechanical and chemical properties

NaI and CsI are both alkali halide compounds so they present good scintillation properties when the pure crystal is doped with certain impurities (normally thalium). NaI is a lower cost material than CsI and is in greater abundance, but is hygroscopic and, therefore, deteriorates through prolonged water absorption into its structure. Since CsI(Tl) is less hygroscopic than NaI(Tl), it becomes more important for applications such as airborne platforms where size and weight are relevant. Also, because it is less brittle than NaI, it can be exposed to more severe conditions of shock and vibration. When activated, the CsI detectors have a larger gamma-ray absorption coefficient per unit size than NaI detectors, making them more applicable for small sized detectors [6]. An alternative scintillation material is the Bismuth Germanate (or BGO) have crystals of reasonable size, with high density and large atomic number compared to others scintillators, which results in the largest probability per unit volume for the photoelectric absorption of gamma rays [6]. Like the majority scintillators, the light output from BGO decreases with increasing temperature. Since the light yield is also low at room temperature (10-20% of that of NaI), it is suddenly decrease in light output becomes BGO useless at high temperature applications. Therefore, BGO is primary interest when there is a need for gamma counting efficiency in detriment of energy resolution. This detector remains two to three times more expensive than NaI [6]. Semiconductor CZT is an alternative to scintillators since it has an energy resolution of 2.0-2.5% and can operate at room temperature, however the volumes are limited to 1 cm³. Neutron detectors are very valuable in the search for fissile materials. Examples are improved ³He ionization counters

and ^6Li loaded phosphors and scintillators.

V. SCENARIOS VS DETECTION SYSTEMS

Table II resumes the detection systems presented in this chapter and the corresponding scenarios which they could be applied.

A. Accidents in nuclear facilities

1) *Scenario Description:* In this scenario it can be included major nuclear accidents or accidental releases from nuclear installations like the recent air release of ruthenium 106 in 2017. Since the spread of radiation can easily extend into several tens of kilometers, in the event of a nuclear catastrophe, a ground-based monitoring system may not be practically applicable due to financial constraints and possible safety and security related issues, and also due to the non-availability of proper roads in remote locations, thick vegetation, abrupt slopes and water passages. An alternative is air-borne detection systems which can be used to monitor high levels of radiation through the use of real-time monitoring methods at safe altitudes [3].

2) *Detection systems described in literature:* After the accident at the FDNPP, initial measurements of radiation intensity, dose and respective spatial distribution were performed, using manned aerial means at altitudes of 150 - 700 m which allowed to quickly understand the approximate distribution of radio-caesium contamination over a very large area. However, according to the Japanese aviation law manned aircrafts are prohibited from flying at altitudes below 150 m preventing better spatial resolution. By lowering the altitude they would also put the crews at risk (contamination and exposure). An unmanned helicopter was also used with a weight of 94kg and a payload of three $\text{LaBr}_3[\text{Ce}]$ scintillators (totaling 6.5 kg) at an altitude of 80 m and a speed of 8 m/s, obtaining an improvement in the spatial resolution[7]. Currently there is a need to do high-resolution radiation mapping to investigate derived contaminant migration and to verify the effectiveness of various remediation methods. To measure the intensity of the radiation fields and radionuclide identification it was used a CZT detector coupled to a multi-rotor at a height of 1 to 5 meters from surfaces and at speeds 1 m/s, which allowed monitoring elevations of land and infrastructure [7], [8], [9].

B. Illicit traffic of Radioactive material and SNM

1) *Scenario Description:* The threat of nuclear terrorism has loomed over the international community for decades. Bad actors may weaponize highly enriched nuclear material into improvised nuclear devices (INDs) capable of great destruction or weaponize radiological material into radiological dispersal devices (RDDs) as Dirty Bombs [10]. Gamma-emitting radioisotopes may be obtained from the industry and medicine such as ^{60}Co , ^{137}Cs , ^{192}Ir .

2) *Detection systems described in literature:* Bandstra et al. (2016) studies includes an examination of the trade-offs between detection through spectroscopy and imaging and suggests that there is a strong correlation between local environment and radiological background. The use of context

and/or environment specific detection thresholds and background models could allow for improved detection sensitivity at a constant false alarm rate. Miller et al. (2015) proposed a small, inexpensive and semiautonomous mobile robot with a LaBr_3 scintillator surrounded by a lead collimator that blocks gamma rays except those along the detector's axial direction. This allows to perform a 180° horizontal scan rotating the detector and a directional profile of gamma radiation count rates is overlaid on top of visual panorama. A cooperative approach between a UGV and UAV was also proposed in order to combine the advantages of both platforms (Lazna, 2018). Recently, in mini-airborne survey we can find in the literature the use BGO gamma-ray spectrometer, with relatively large volume (103 cm^3). This detector system which weights with batteries included 4 kg provides about 300 times greater sensitivity in comparison with the 1 cm^3 CZT semiconductor detector used in many previous UAV surveys in environmental applications. Detection of SNM typically relies on gamma and neutron radiation. The detection of nuclear materials is complicated by the many potential entryways or transport modes available for smuggling. Additionally, the radiation signals detected from these materials are relatively weak and especially difficult to detect at distance (e.g., the neutron emission from a Highly Enriched Uranium) [10]. Detection and interpretation of gamma-ray signals are typically easier than that for neutrons, due to the detection equipment used, relative ease of obtaining gamma spectrometry data, the need for radiation-type discrimination in neutron detection, and use of thermalization mediums for neutron detection. However, gamma-ray detection of threat materials is complicated by the much higher prevalence of gamma-ray emitting, for example due to NORM (bananas- ^{40}K or cat litter ^{232}Th decay chain). NORM may cause unacceptable rates of false alarms in detector systems or may be utilized to mask the signal from threat materials. Additional complications are added due to the relative ease of gamma-ray shielding, which may be accomplished with a few centimeters of high-Z materials such as lead and unavoidably by the frame and siding of vehicles. Finally and importantly, the signal received by the detector from a threat source may be masked by gamma-ray background radiation, which is approximately an order of magnitude higher for gamma rays than neutrons [10]. It is possible to detect Weapons grade Plutonium (WgPu) using neutron detection systems at a distance less than 15 meters. However is very difficult to detect Weapons grade Uranium (WgU) using both neutron and gamma detectors, so it is necessary to use active interrogation techniques using tagged neutrons [11].

C. NORM

1) *Scenario Description:* Since natural radiation is the largest contributor of external dose to the world population, the study of gamma radiation from natural sources is of particular importance [12]. NORM is used in this article to encompass all NORM where human activities have increased the potential for exposure in comparison with the unaltered

TABLE II
LITERATURE REVIEW OF MOBILE DETECTOR SYSTEMS VS SCENARIOS

Radiation Detectors other equipment	Platform	Application	Possible Scenario & Ref.
2 BGO (103 cm ³ each)	UAV	Mini-airborne survey	A, B [21]
He-3 detector; NaI scintillator; 4 GM tubes / Visual and Hyperspectral; LIDAR;GPS	Manned Ground-Vehicle	Search radioact. sources in urban environ. (nuclear security)	B [16]
LaBr ₃ scintillation w/ lead sheath / Visual imagery	Small UGV	Trace local point gamma sources	B [17]
Pair of 2in. NaI scintillator w/ lead shielding	UGV/ UAV for 3D map	Localization of gamma sources (hotspots)	B [18]
He-3 proportional counter with moderator; NE-213 liquid-scintillator; LaBr(Ce) and NaI scintillators	Mobile multi-detector system	Prevention of illicit trafficking of Nuclear and radioactive materials	B [20]
lithium glass GS10 inorganic, EJ-204 plastic and CsI(Tl) inorganic scintillators	Portable imager	Detect and localise gammas, thermal and fast neutrons: Compton and neutron scatt.	B [19]
2 He-3 (5 cm moderator); 2 plastic scintillators BC412; 3in. NaI scintillator / GPS	Manned Ground-Vehicle	Search and detection of nuclear and radioactive materials during road transport	B [22]
1in. NaI scintillator	Hand-held	NORM mapping	C [12]
CZT coplanar-grid (100 mm ³) / GPS, LIDAR	Small UAV	Mapping	A, C [14], [15], [7], [8], [9]

situation. Human activities that exploit these resources may lead to enhanced concentrations of radionuclides (often referred to as technologically enhanced NORM (TE-NORM)) and (or) enhanced potential for exposure to naturally occurring radioactive materials in products, by-products, residues and wastes. Such activities may include, for instance, the mining and processing of ores, the combustion of fossil fuels, or the production of natural gas and oil [13].

2) *Detection systems described in literature:* Gamma ray spectrometer CZT (GR1 Kromek) coupled to a low cost, lightweight UAV with GPS and LIDAR was used to obtain a high resolution maps of radiological contamination in the environment and to produce mapping of legacy uranium mines [14], [15]. Since the platform is at low altitude, sensitivity of the radiation detection measurement is significantly increased, therefore allowing small and low weight detectors to be used [14].

VI. RECENT ADVANCES AND PERSPECTIVES

Active research is in progress to obtain good energy resolution high-Z sensitized plastic scintillators (which is available in large volumes) by mixing it with fluoride and oxide nano-particles. In particular, CsPbBr₃, a halide perovskite, has been demonstrated to have an excellent energy resolution of 3.8% [5].

Since there several detection systems and platforms it is necessary standards in order to see if they comply with it. Relative to mobile systems there are International and American Standards for performance requirements for hand-held and American Standards for vehicle mounted detectors (ground-based) in Homeland security [24], [25], [26]. However, to the best of our knowledge, there is no Standards for air-based Mobile detection systems. International Atomic Energy Agency (IAEA) also published in 1999 generic procedures for monitoring in a nuclear or radiological emergency. Since then many new developments were achieved

in the field of radiation detector systems and platforms like Unmanned vehicles.

VII. CONCLUSIONS

Depending on the scenario (e.g. source term), the monitoring purpose (detection, localization, identification and/or mapping) and the operational environment (e.g. weather, topography) one can choose the best platform or combination of platforms and radiation detection system. Where radiation can be too risky for human or the task is too demanding it can be used unmanned vehicles. However this last choice can have some drawbacks like communication problems, autonomy and payload limitations.

The available volume sizes and detector sensitivity makes the scintillator detectors a good choice to be applied in all three scenarios. Some scintillators used in mobile Monitoring systems are NaI(Tl), CsI(Tl) LaBr₃[Ce] and BGO. However, when lighter detectors (< 1kg) are needed CsI(Tl) scintillator and CZT semiconductor are available and with good energy resolution. For SNM detection it is necessary to apply both neutron and gamma measurements.

Future work is needed in Mobile Radiation Measurements specially in the definition of performance requirements for monitoring and sampling detectors coupled to aerial-based platforms, in particular UAVs. Detection systems for UAVs should be light, robust, low rate of false alarms and with good energy resolution, counting efficiency and dead time.

ACKNOWLEDGMENT

IPFN activities received financial support from “Fundação para a Ciência e Tecnologia” through projects UIDB/50010/2020 and UIDP/50010/2020. This paper is also part of the project FRIENDS - Fleet of dRones for radIological inspEction, commuNication anD reScue, supported by the FCT, Compete 2020 and Lisboa 2020 under

the PORTUGAL 2020 Partnership Agreement, through the European Regional Development Fund (ERDF).

REFERENCES

- [1] F. E. Schneider, B. Gaspers, K. Peräjärvi, and M. Gärdestig, "Possible scenarios for radiation measurements and sampling using unmanned systems : ERNCIP thematic group Radiological and nuclear threats to critical infrastructure Task 3 deliverable 2", no. March, 2015, doi: 10.2788/60148.
- [2] R. Kouzes et al., "Alternatives to ^3He for Neutron Detection for Homeland Security," no. March 2015, 2010.
- [3] D. Connor, P. G. Martin, T. B. Scott, P. G. Martin, and T. B. S. Airborne, "Airborne radiation mapping : overview and application of current and future aerial systems", *Int. J. Remote Sens.*, vol. 37, no. 24, pp. 5953–5987, 2016, doi: 10.1080/01431161.2016.1252474.
- [4] J. Lahtinen and N. S. Authority, "Emergency Monitoring Strategy and Radiation Measurements Working Document of the NKS Project Emergency Management and Radiation Monitoring in Nuclear and Radiological Accidents (EMARAD)", no. April, 2006.
- [5] K. A. Pradeep Kumar, G. A. Shanmugha Sundaram, and R. Thiruvengadathan, "Advances in detection algorithms for radiation monitoring", *J. Environ. Radioact.*, vol. 217, no. January, p. 106216, 2020, doi: 10.1016/j.jenvrad.2020.106216.
- [6] F. Knoll, *Radiation detection and measurement*, John Wiley & Sons, 2010.
- [7] P. G. Martin, O. D. Payton, J. S. Fardoulis, D. A. Richards, Y. Yamashiki, and T. B. Scott, "Low altitude unmanned aerial vehicle for characterising remediation effectiveness following the FDNPP accident," *J. Environ. Radioact.*, vol. 151, pp. 58–63, 2016, doi: 10.1016/j.jenvrad.2015.09.007.
- [8] P. G. Martin, O. D. Payton, Y. Yamashiki, D. A. Richards, and T. B. Scott, "High-resolution radiation mapping to investigate FDNPP derived contaminant migration," *J. Environ. Radioact.*, vol. 164, pp. 26–35, 2016, doi: 10.1016/j.jenvrad.2016.06.025.
- [9] P. G. Martin et al., "3D unmanned aerial vehicle radiation mapping for assessing contaminant distribution and mobility", *Int. J. Appl. Earth Obs. Geoinf.*, vol. 52, pp. 12–19, 2016, doi: 10.1016/j.jag.2016.05.007.
- [10] B. E. Cazalas, "Defending Cities Against Nuclear Terrorism: Analysis of A Radiation Detector Network for Ground Based Traffic", vol. 14, no. December, 2018.
- [11] S. Fetter, V. A. Frolov, M. Miller, R. Mozley, O. F. Prilutsky, S. N. Rodionov, and R. Z. Sagdeevb, "Detecting Nuclear Warheads", *Sci. Glob. Secur.*, vol. 1, no. 3–4, pp. 225–253, 1990, doi: 10.1080/08929889008426333.
- [12] N. N. Garba, A. T. Ramli, M. A. Saleh, S. M. Sanusi, and H. T. Gabdo, "Radiological mapping of Kelantan, Malaysia, using terrestrial radiation dose rate", *Isotopes Environ. Health Stud.*, vol. 52, no. 3, pp. 214–218, 2016, doi: 10.1080/10256016.2016.1095189.
- [13] International Atomic Energy Agency, "Nuclear Security Systems and Measures for the Detection of Nuclear and Other Radioactive Material out of Regulatory Control: Implementing Guide", IAEA Nuclear Security Series no. 21, 2013.
- [14] J. W. MacFarlane et al., "Lightweight aerial vehicles for monitoring, assessment and mapping of radiation anomalies," *J. Environ. Radioact.*, vol. 136, pp. 127–130, 2014, doi: 10.1016/j.jenvrad.2014.05.008.
- [15] P. G. Martin, O. D. Payton, J. S. Fardoulis, D. A. Richards, and T. B. Scott, "The use of unmanned aerial systems for the mapping of legacy uranium mines," *J. Environ. Radioact.*, vol. 143, pp. 135–140, 2015, doi: 10.1016/j.jenvrad.2015.02.004.
- [16] M. S. Bandstra et al., "RadMAP: The Radiological Multi-sensor Analysis Platform" *Nucl. Inst. Methods Phys. Res. A*, vol. 840, no. September, pp. 59–68, 2016, doi: 10.1016/j.nima.2016.09.040.
- [17] A. Miller, R. Machrafi, and A. Mohany, "Development of a semi-autonomous directional and spectroscopic radiation detection mobile platform," *Radiat. Meas.*, vol. 72, pp. 53–59, 2015, doi: 10.1016/j.radmeas.2014.11.009.
- [18] T. Lazna, P. Gabrlík, T. Jilek, and L. Zalud, "Cooperation between an unmanned aerial vehicle and an unmanned ground vehicle in highly accurate localization of gamma radiation hotspots", *Int. J. Adv. Robot. Syst.*, vol. 15, no. 1, pp. 1–16, 2018, doi: 10.1177/1729881417750787.
- [19] H. Al, D. Cheneler, and S. D. Monk, "A fast and portable imager for neutron and gamma emitting radionuclides", *Nucl. Inst. Methods Phys. Res. A*, vol. 953, no. September 2019, p. 163253, 2020, doi: 10.1016/j.nima.2019.163253.
- [20] D. Cester et al., "Special nuclear material detection with a mobile multi-detector system", *Nucl. Inst. Methods Phys. Res. A*, vol. 663, no. 1, pp. 55–63, 2012, doi: 10.1016/j.nima.2011.10.011.
- [21] O. Šálek, M. Matolín, and L. Gryc, "Mapping of radiation anomalies using UAV mini-airborne gamma-ray spectrometry," *J. Environ. Radioact.*, vol. 182, no. November 2017, pp. 101–107, 2018, doi: 10.1016/j.jenvrad.2017.11.033.
- [22] S. Kwak, S. Chang, and H. Yoo, "Radiation Detection System for Prevention of Illicit Trafficking of Nuclear and Radioactive Materials," *J. Radiat. Prot.*, vol. 35, no. 4, pp. 167–171, 2010.
- [23] I. Atomic and E. Agency, "Generic procedures for monitoring in a nuclear or radiological emergency", no. June, 1999.
- [24] "Radiation protection instrumentation – Hand-held instruments for the detection and identification of radionuclides and for the indication of ambient dose rate equivalent rate from photon radiation", in *International Standard IEC 62327:2017 (Revision of IEC 62327:2006)*, 15 Dec. 2017.
- [25] "American National Standard Performance Criteria for Handheld Instruments for the Detection and Identification of Radionuclides", in *ANSI N42.34-2015 (Revision of ANSI N42.34-2006)*, pp.1-60, 24 Aug. 2016.
- [26] "American National Standard Performance Criteria for Mobile and Transportable Radiation Monitors Used for Homeland Security", in *ANSI N42.43-2016 (Revision of ANSI N42.43-2006)*, vol., no., pp.1-54, 25 May 2016.



